J. Fluid Mech. (2013), *vol.* 716, *pp.* 137–170. © Cambridge University Press 2013
doi:10.1017/jfm.2012.526

Modelling single- and tandem-bubble dynamics between two parallel plates for biomedical applications

C.-T. Hsiao[1],†, J.-K. Choi[1], S. Singh[1], G. L. Chahine[1], T. A. Hay[2], Yu. A. Ilinskii[2], E. A. Zabolotskaya[2], M. F. Hamilton[2], G. Sankin[3], F. Yuan[3] and P. Zhong[3]

[1]Dynaflow, Inc., 10621-J Iron Bridge Rd., Jessup, MD 20794, USA

[2]Applied Research Laboratories, The University of Texas at Austin, Austin, TX 78713, USA

[3]Department of Mechanical Engineering and Materials Science, Duke University, Box 90300, NC 27708, USA

(Received 25 January 2012; revised 9 October 2012; accepted 21 October 2012)

Carefully timed tandem microbubbles have been shown to produce directional and targeted membrane poration of individual cells in microfluidic systems, which could be of use in ultrasound-mediated drug and gene delivery. This study aims at contributing to the understanding of the mechanisms at play in such an interaction. The dynamics of single and tandem microbubbles between two parallel plates is studied numerically and analytically. Comparisons are then made between the numerical results and the available experimental results. Numerically, assuming a potential flow, a three-dimensional boundary element method (BEM) is used to describe complex bubble deformations, jet formation, and bubble splitting. Analytically, compressibility and viscous boundary layer effects along the channel walls, neglected in the BEM model, are considered while shape of the bubble is not considered. Comparisons show that energy losses modify the bubble dynamics when the two approaches use identical initial conditions. The initial conditions in the boundary element method can be adjusted to recover the bubble period and maximum bubble volume when in an infinite medium. Using the same conditions enables the method to recover the full dynamics of single and tandem bubbles, including large deformations and fast re-entering jet formation. This method can be used as a design tool for future tandem-bubble sonoporation experiments.

Key words: biological fluid dynamics, biomedical flows, bubble dynamics

1. Introduction

Inertial cavitation, which is the explosive growth, collapse, and dynamics of vapour/gas bubbles in an aqueous medium due to large pressure fluctuations, plays an important role in a diverse range of engineering (Arndt 1981; Chahine 1982; Blake & Gibson 1987; Haines *et al.* 2005) and biomedical (Miller 1987; Haubold,

† Email address for correspondence: chao_tsung@hotmail.com

https://doi.org/10.1017/jfm.2012.526 Published online by Cambridge University Press

Ely & Chahine 1994; Chahine 1996; Zhong *et al.* 1997; Zhong *et al.* 2001; Pishchalnikov *et al.* 2003; Gracewski, Miao & Dalecki 2005; Miao, Gracewski & Dalecki 2008; Chen *et al.* 2011) applications. Among the emerging biomedical applications, ultrasound-mediated drug, gene and siRNA delivery have been shown to be enhanced by the presence of cavitation bubbles (Mitragotri 2005). It is believed that cavitation bubbles produced during sonoporation can cause temporary openings in the cell membrane to allow a particulate drug to enter the cell. However, the fundamental mechanism by which cavitation produces membrane poration at the cellular level is still poorly understood.

Motivated by the success of ultrasound-mediated drug/gene delivery and the desire to better understand the mechanisms of sonoporation, laser-generated tandem microbubbles, conventionally used to simulate cavitation bubbles (Lauterborn & Bolle 1975; Kroninger *et al.* 2010), were utilized to produce directional and targeted membrane poration of individual cells in microfluidic systems (Sankin, Yuan & Zhong 2010). By confining the bubble generation and interaction in a narrow fluid gap ($\sim$25 μm) between two solid plates, this new approach enables a clear and precise observation of bubble–bubble interaction and microjet formation. The experiments showed that a single bubble did not form a re-entrant jet toward a nearby cell and thus no membrane poration was observed. However, by introducing a second bubble with appropriate delay time and location, the first bubble was driven to form a re-entrant jet toward the cell, leading to localized and directional membrane poration (Sankin *et al.* 2010).

However, even with state-of-the-art ultra-high-speed cameras at a framing rate of up to 200 million frames per second, an experimental study would be able to only capture limited details of jet development and impact near the end of the bubble collapse owing to the microscopic scale and extreme speed of the phenomena. To complement the experimental observations, accurate numerical modelling of tandem-microbubble interaction in a confined domain is essential.

Although many previous numerical studies have addressed bubble–bubble and bubble–wall interaction (Shima & Tomita 1981; Blake & Gibson 1987; Chahine 1993; Tomita, Sato & Shima 1994; Tomita *et al.* 2002; Gracewski *et al.* 2005; Krieger & Chahine 2005; Calvisi, Iloreta & Szeri 2008; Iloreta, Fung & Szeri 2008; Miao *et al.* 2008; Lim *et al.* 2010), most of them did not concern a confined domain. Some early work (Chahine & Morine 1980; Shima & Sato 1980; Chahine 1982; Chahine & Liu 1985) addressed bubble dynamics in confinement from experimental and analytical viewpoints prior to recent advances in numerical and analytical techniques. Recent numerical work studying bubbles in a confined environment includes bubbles between two confined plates and in tubular vessels (Cui *et al.* 2006; Wilson 2010; Chen *et al.* 2011; Leighton 2012). Technically, the tandem-microbubble interaction in a narrow gap between two rigid or deforming walls presents particular challenges because of its three-dimensional nature, which requires advanced analytical and/or numerical procedures. This is especially true as the boundaries of the bubbles and plates can become extremely close during the bubble expansion, and the bubble deforms, resulting in microscopic re-entrant jets, which modify the topology of the bubbles.

In this communication, we develop and compare two simulation approaches to describe the dynamic behaviour of the interacting bubbles in the presence of rigid boundaries. The first approach is based on potential flow and uses the boundary element method (BEM) for both axisymmetric and full three-dimensional geometries (Chahine & Duraiswami 1993; Chahine, Duraiswami & Kalumuck 1997; Hsiao, Lu & Chahine 2010) for single- and tandem-bubble dynamics between two finite circular

https://doi.org/10.1017/jfm.2012.526 Published online by Cambridge University Press

rigid plates. Descriptions of the bubble surfaces are obtained as part of the solution procedure, in order to capture full non-spherical deformations and potential bubble splitting, and/or formation and development of re-entrant jets due to bubble–bubble and bubble–wall interactions. The second approach is semi-analytic and accounts for fluid compressibility, elasticity of the plates, and a viscous boundary layer in the channel, but limits the bubble dynamics to spherical pulsations (Hay *et al.* 2012). The study, while ultimately seeking to recover experimentally available results from Sankin *et al.* (2010) and to help design future experiments, aims at understanding through analysis and parametric studies the importance of the various physical quantities controlling the bubble dynamics between two close boundaries. Comparisons between simulation results obtained from the two models, as well as with experimental measurements, will help evaluate the importance of the various physical quantities either modelled or ignored by each approach.

2. Experimental procedures and results

The experimental setup for producing tandem-microbubble interaction with resultant directional jet formation and membrane poration has been described in detail in our previous study (Sankin *et al.* 2010). Briefly, two 5 ns pulsed lasers were focused through a 63X microscope objective into a narrow fluid gap of 25 μm width filled with 0.4 % Trypan blue, which preferentially absorbed the incident laser energy and thus generated individual microbubbles of 50 μm maximum diameter via optical breakdown. The two laser beams were aligned carefully so that their foci were separated by 40 μm. By releasing the second laser 4 μs after the first one, tandem microbubbles in anti-phase oscillation can be produced, leading to asymmetric deformation and jet formation in opposite directions (see figure 22 described later). The dynamics of bubble–bubble interaction in the middle plane parallel to the narrow fluid gap were captured using an ultra-high-speed camera (Imacon 200, DRS Hadland) at a framing rate of 1 million frames/second with 50 ns exposure time.

3. Solution methods

3.1. *Large-free-surface-deformation boundary element model*

Highly inertial bubbles, such as in cavitation or generated by laser or electric spark discharge or explosives, have been commonly modelled using potential inviscid and incompressible models (Knapp, Daily & Hammitt 1970; Plesset & Prosperetti 1977; Blake & Gibson 1987; Brennen 1995). This is usually justified by the fact that the bubble wall speed is relatively very large although the flow around the bubble is largely subsonic. Viscous effects in the bulk of the liquid (i.e. far from walls) are usually neglected and are sometimes accounted for in the boundary conditions at the bubble wall. While these assumptions have been proven valid for larger than millimetre-sized bubbles, they remain to be validated for the micron-sized bubbles and in the confinement between two walls of interest here. This study should help elucidate the limits of validity of these assumptions.

The present study uses the BEM module of 3DynaFS© (Chahine 1991; Hsiao & Chahine 2010), which has been extensively used for cavitation, underwater explosions, microscopic bubbles, and free surface waves (Chahine, Perdue & Tucker 1989, Chahine *et al.* 1992, Chahine & Duraiswami 1993; Zhang, Duncan & Chahine 1993; Chahine 1994, 1995; Chahine *et al.* 1997; Chahine 2005; Gracewski *et al.* 2005; Hsiao *et al.* 2010). The liquid flow due to the bubble dynamics is assumed to be irrotational and incompressible. The assumption of irrotational flow allows the definition of a

https://doi.org/10.1017/jfm.2012.526 Published online by Cambridge University Press

velocity potential, ϕ, such that

$$u = \nabla\phi, \tag{3.1}$$

where $\boldsymbol{u}$ is the velocity vector. The assumption that the liquid is incompressible leads to Laplace's equation for the potential:

$$\nabla^2\phi = 0. \tag{3.2}$$

A BEM is used to solve (3.2). This method is based on an integral solution of the Laplace equation using the Gauss–Ostrogradsky divergence theorem, which can be written using Green's second identity:

$$\int_V (\phi\nabla^2 G - G\nabla^2\phi)\,\mathrm{d}V = \int_S \boldsymbol{n}\cdot[\phi\nabla G - G\nabla\phi]\,\mathrm{d}S. \tag{3.3}$$

In this expression V is the three-dimensional domain of integration having elementary volume $\mathrm{d}V$. The boundary surface of V is S, the outer surface of the domain plus the sum of the surfaces of all inclusions, here the bubbles. S has an elementary surface $\mathrm{d}S$ with local normal unit vector $\boldsymbol{n}$.

The velocity potential ϕ is harmonic in the fluid domain, and G is Green's function. If G is selected to be harmonic everywhere except at some discrete points, (3.3) simplifies considerably. For instance, if

$$G = -\frac{1}{|\boldsymbol{x}-\boldsymbol{y}|}, \tag{3.4}$$

where $\boldsymbol{x}$ is a fixed point in V and is $\boldsymbol{y}$ is a point on the boundary surface S, (3.3) reduces to Green's formula with $\alpha\pi$ being the solid angle at $\boldsymbol{x}$ under which the domain V is seen:

$$\Omega\phi(\boldsymbol{x}) = \int_S \boldsymbol{n}_y\cdot[\phi(\boldsymbol{y})\nabla G(\boldsymbol{x},\boldsymbol{y}) - G(\boldsymbol{x},\boldsymbol{y})\nabla\phi(\boldsymbol{y})]\,\mathrm{d}S, \tag{3.5}$$

$$\Omega\begin{cases} =4\pi & \text{if } \boldsymbol{x} \text{ is a point in the fluid} \\ =2\pi & \text{if } \boldsymbol{x} \text{ is a point on a smooth surface} \\ >4\pi & \text{if } \boldsymbol{x} \text{ is a point at a sharp corner of the discretized surface.} \end{cases} \tag{3.6}$$

This equation states that if the velocity potential ϕ and its normal derivatives are known on the boundary surface S of a domain V, where ϕ satisfies the Laplace equation, then ϕ can be determined anywhere in V by integration over the boundary surface. Using this expression the BEM reduces by one the dimension of the problem of solving the Laplace equation.

To solve (3.5) with the BEM numerically, all boundaries are discretized into triangles or quadrilateral panels, S_k, and the surface integrals are evaluated at any field point $\boldsymbol{x}$ as a summation over all panels of the influence of singularity distributions over the boundaries. This enables one to write Green's second formula, (3.5), in the form

$$a\pi\phi(x) = \sum_{k=1}^{P}\int_{S_k}\left(\phi(y)\frac{\partial G}{\partial n}(x,y) - G(x,y)\frac{\partial\phi}{\partial n}(y)\right)\mathrm{d}S_k, \tag{3.7}$$

where P is the number of surface panels on the boundary. To evaluate the integrals over S_k, given in (3.7), it is necessary to assume a relationship between the values of ϕ and $\partial\phi/\partial n$ at a surface point and their values at the discretized nodes. Here, we

https://doi.org/10.1017/jfm.2012.526 Published online by Cambridge University Press

assume that these quantities vary linearly over a panel and can be described by the values at the panel nodes. Each integral over a discretized panel can then be written as a linear combination of the values of ϕ or $\partial\phi/\partial n$ at the surrounding nodes. The expressions for these integrals are complex, and details can be found in an earlier study (Miller 1987). With the integration over each panel performed, the discretized (3.7) can be expressed as

$$a\pi\phi_j = \sum_{k=1}^{P}\sum_{i=1}^{m}\left[B_i^k\phi_i^k - A_i^k\left(\frac{\partial\phi}{\partial n}\right)_i^k\right], \quad j = 1, N, \tag{3.8}$$

where ϕ_i^k and $(\partial\phi/\partial n)_i^k$ are the potential and its normal derivative at node i of panel k, $\boldsymbol{A}_i^k$ and B_i^k are influence coefficients obtained from the elementary integrations, N is the total number of nodes, P is the total number of panels and the constant $m = 3$ (triangular element) or 4 (quadilateral element).

Following a 'collection' procedure, in which the contributions due to the same node are collected from the various contiguous panels and summed up, (3.8) can be rewritten as

$$a\pi\phi_j = \sum_{i=1}^{N}\left[\bar{B}_i\phi_i - \bar{A}_i\left(\frac{\partial\phi}{\partial n}\right)_i\right], \quad j = 1, N, \tag{3.9}$$

where $\bar{A}$ and $\bar{B}$ are the altered influence coefficients due to summation of panels around the same node. It is noted that the 'collection' approach transfers the panel contributions in (3.8) to node contributions in (3.9). Equation (3.9) can be expressed in matrix form as

$$\bar{\boldsymbol{B}}\frac{\partial\phi}{\partial n} = (a\pi\boldsymbol{I} + \bar{\boldsymbol{A}})\phi, \tag{3.10}$$

where $\boldsymbol{I}$ is the $N \times N$ identity matrix, and $\bar{\boldsymbol{A}}$ and $\bar{\boldsymbol{B}}$ are $N \times N$ influence coefficient matrices. With ϕ known on all boundary nodes, (3.10) is a linear system of N equations and can be readily solved for N unknowns of $\partial\phi/\partial n$, using classical methods such as LU decomposition and Gauss elimination.

3.1.1. *Initial conditions*

3DynaFS© starts bubble computations using an initially spherical bubble of radius R_0. The initial conditions are selected to correspond to either an initial static equilibrium if this is the case, or to the dynamic of a spherical bubble up to the start of the 3DynaFS-BEM© computations if the initial conditions are dynamic such as with a spark-generated or laser-generated bubble. This is further discussed below.

The dynamics of a spherical bubble oscillating in an otherwise quiescent liquid at ambient pressure, P_{amb}, are given by the Rayleigh–Plesset equation:

$$\rho\left[R\ddot{R} + \frac{3}{2}\dot{R}^2\right] = P_{g0}\left(\frac{R_0}{R}\right)^{3k} + P_v - P_{amb} - \frac{2\sigma}{R}, \tag{3.11}$$

where $R(t)$ is the bubble radius at time t, ρ is the liquid density, and σ is the surface tension coefficient. A dot over a symbol represents differentiation with respect to time. P_v is the liquid vapour pressure at the ambient temperature, and P_{g0} is the partial pressure of the gas inside the bubble when it has the radius R_0. The gas pressure is assumed to be connected to the bubble volume through a polytropic compression law

https://doi.org/10.1017/jfm.2012.526 Published online by Cambridge University Press

with constant k such that:

$$P_g R^{3k} = P_{g0} {R_0}^{3k}. \tag{3.12}$$

Equation (3.11) can be integrated to give for $k \neq 1$ the following expression for the bubble wall velocity, $\dot{R}$:

$$\dot{R} = \sqrt{\frac{2}{\rho}} \left[\frac{P_g}{3(1-k)} (1 - \varepsilon^{3k-3}) + \frac{P_v - P_{amb}}{3} (1 - \varepsilon^{-3}) - \frac{\sigma}{R} (1 - \varepsilon^{-2}) \right]^{1/2}, \tag{3.13}$$

where $\varepsilon = R/R_{max}$ with R_{max} being the maximum value the spherical bubble radius will attain. A similar equation exists for $k = 1$.

Equation (3.13) can be used to provide an initial condition to the 3DYNAFS© computations assuming that nearby boundary effects have not had time to become significant before $t = 0$. This is obviously an approximation for bubble generation near pre-existing objects or bubbles (such as tandem bubbles and walls here) but unless one is interested just in the first microseconds of the behaviour, the numerical computations adapt very fast to any errors in the initial conditions, and time steps are very significantly reduced at the introduction of a new bubble to minimize the duration of the transient.

If the initial and maximum bubble sizes, R_0 and R_{max}, are known (e.g. from experimental observations of the unbounded bubble behaviour for the same energy deposit), then specifying P_{g0} enables the initial wall velocity $\dot{R}_0$ to be found from (3.13), with $\varepsilon = \varepsilon_0 = R_0/R_{max}$ and $P_g = P_{g0}$.

The velocity potential of the corresponding flow field is then that of a point source of intensity $4\pi R_0^2 \dot{R}_0$. Its value decays inversely with distance r from the bubble centre and is therefore given at a distance r by

$$\phi = -R^2 \dot{R}/r. \tag{3.14}$$

At the bubble wall, $r = R_0$, we therefore have

$$\phi(R_0) = -\dot{R}_0 / R_0. \tag{3.15}$$

When selecting $R_0 = R_{min}$ (where R_{min} is the minimum bubble radius), the initial potential and bubble wall velocity, $\dot{R}_0$, are zero. Equation (3.13) then provides the following initial value of P_{g0}, with $\epsilon_* = R_{min}/R_{max}$:

$$P_{g0} = \frac{3(1-k)}{1 - {\varepsilon_*}^{3k-3}} \left[\frac{P_{amb} - P_v}{3} (1 - {\varepsilon_*}^{-3}) + \frac{\sigma}{R} (1 - {\varepsilon_*}^{-2}) \right]. \tag{3.16}$$

For a choice of the initial radius that is different from R_{min} or R_{max}, a non-zero value of the bubble wall velocity given by (3.13) should be used. A failure to do so can lead to significant quantitative errors in the computed bubble behaviour.

3.1.2. *Boundary conditions*

The mathematical modelling of free-surface dynamics leads to a boundary value problem posed for a domain with moving boundaries on which nonlinear boundary conditions should be satisfied. At a point x_S on any boundary S_B, the boundary conditions are the continuity of the normal stress components and the condition that the fluid normal velocity equals the interface normal velocity,

$$\nabla\phi \cdot \boldsymbol{n} = \boldsymbol{u}_S \cdot \boldsymbol{n}, \tag{3.17}$$

https://doi.org/10.1017/jfm.2012.526 Published online by Cambridge University Press

where $\boldsymbol{u}_S$ is the boundary velocity and $\boldsymbol{n}$ is the local unit normal to the boundary. For a solid non-deformable, non-moving boundary, this condition degenerates to

$$\nabla\phi \cdot \boldsymbol{n} = 0. \tag{3.18}$$

3.1.3. *Bubble content equations*

The pressure inside each bubble is assumed spatially homogeneous, and the gas inside each bubble is assumed to be composed of both vapour of the liquid and non-condensible gas. The pressure at any instant is given by the sum of the partial pressures of the liquid vapour and of the non-condensible gases. Vaporization of the liquid is assumed to occur at a fast enough rate so that the vapour pressure inside the bubble remains equal to the equilibrium liquid vapour pressure at the ambient temperature. The non-condensible gas of pressure P_g is assumed to satisfy the polytropic law,

$$P_g V^k = \text{constant}, \tag{3.19}$$

where $V(t)$ is the volume of the bubble at time t, and k is the polytropic exponent. This leads to the following form of the normal stress boundary condition:

$$P_l = P_v + P_{g0}\left[\frac{V_0}{V(t)}\right]^k - \sigma C, \tag{3.20}$$

where V_0 is the initial volume of the bubble and C is the local surface curvature given by

$$C = \nabla \cdot \boldsymbol{n}, \tag{3.21}$$

The local normal at the surface is defined by

$$\boldsymbol{n} = \pm\frac{\nabla f}{|\nabla f|}, \tag{3.22}$$

where f is a local description of the surface. The appropriate sign is chosen so that all normals point toward the liquid domain.

3.1.4. *Boundary surface update*

To advance the points on the bubble surface the velocity at the nodes is required. The normal velocity is known from the solution of the integral equation while the tangential velocity is obtained by using a local surface fit to the velocity potential ϕ. Since with a potential flow there are no constraints on the tangential velocities, and the only condition one needs to satisfy is (3.17), the user has the option of moving the nodes with the fluid velocity $\nabla\phi$ or with any velocity given by

$$\boldsymbol{u} = \frac{\partial\phi}{\partial n}\boldsymbol{n} + \alpha\frac{\partial\phi}{\partial s}\boldsymbol{t}, \tag{3.23}$$

where $\boldsymbol{n}$ is the unit vector in the normal direction at the boundary and $\boldsymbol{t}$ is the unit vector in the tangential direction. The quantity α is a user-defined input parameter. It should be noted that $\alpha \neq 1$ is an artificial situation. In essence, the node no longer tracks a particle of fluid – that is, if the fluid were real, not potential, and if no-slip were allowed. By selecting different values of α, the user can have some control over the evolution of the grid structure and reduce the accumulation of nodes at certain locations while at the same time satisfying the physical constraints of the potential

https://doi.org/10.1017/jfm.2012.526 Published online by Cambridge University Press

flow assumption. The nodes are then advanced according to

$$\frac{\mathrm{D}\boldsymbol{x}}{\mathrm{D}t} = \boldsymbol{u}. \tag{3.24}$$

To advance the potential in a Lagrangian fashion we need to evaluate

$$\frac{\mathrm{D}\phi}{\mathrm{D}t} = \frac{\partial \phi}{\partial t} + \boldsymbol{u} \cdot \nabla \phi. \tag{3.25}$$

Using Bernoulli's equation and the balance-of-pressures condition at the surface, (3.20), we obtain for $\alpha = 1$:

$$\frac{\mathrm{D}\phi}{\mathrm{D}t} = \frac{1}{\rho}\left[P_\infty - P_v - P_{g0}\left(\frac{V_0}{V(t)}\right)^k - \sigma C\right] + \frac{1}{2}|\nabla\phi|^2. \tag{3.26}$$

3.1.5. *Time stepping*

The 3DYNAFS-BEM© version used here uses a simple Euler stepping scheme to numerically integrate (3.26). The value of a quantity q at time $t + \delta t$ is obtained from known value at time t as

$$q(t + \delta t) = q(t) + \frac{\mathrm{d}q}{\mathrm{d}t}(t)\delta t. \tag{3.27}$$

The choice of the quantity δt is made using an adaptive scheme that ensures that smaller time steps are chosen when rapid changes in the velocity potential occur, while larger ones are chosen for less rapid changes. The user controls this by prescribing the time factor, T_f. The time step is determined as

$$\delta t = \frac{\Delta l_{min}}{25 V_{max}} T_f, \tag{3.28}$$

where V_{max} is the normalized maximum of all computed nodal velocities obtained by the program at the current step and Δl_{min} is the minimum distance between the nodes. The factor 25 in the denominator has been found to provide good results.The user can change this factor by multiplying it with the time scale factor, T_f.

To prevent excessively small steps or large steps leading to inordinately long run times or erroneous results, the time step size is not allowed to become smaller or larger than prescribed minimum and maximum values.

The computation is started with smaller time steps to assure accuracy during this period of very rapid bubble growth. For the first 40 steps after introduction of any new bubble, the time interval is a linear function of the step number k, and is determined as follows:

$$\Delta t = \min(\tfrac{1}{3} k\, \Delta t_{min}, \delta t), \tag{3.29}$$

where Δt_{min} is the minimum time step set in the program, and δt is the time step size calculated from the adaptive method using the minimum panel size and maximum nodal velocity (3.28).

3.2. *Mathematical model*

3.2.1. *General formulation*

Alternatively, the constraining influence of the microfluidic device surfaces on the bubble dynamics, the compressibility of the liquid, the compliance of the walls, and the viscous boundary layers along the walls, may be taken into account using a

https://doi.org/10.1017/jfm.2012.526 Published online by Cambridge University Press

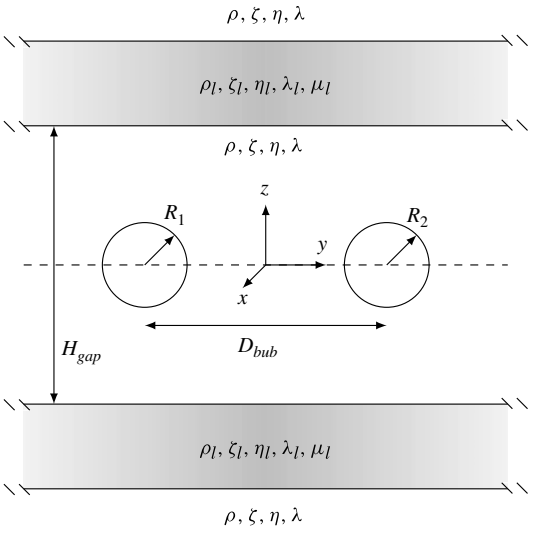


FIGURE 1. Geometry for the UT model.

Green's function approach developed at the University of Texas at Austin (UT). The Green's function approach (UT model) describes the state of the fluid and surrounding viscoelastic media in response to a point source located in a liquid channel, corresponding to a bubble that pulsates in a microfluidic device. The same Green's function, evaluated at different locations, can be used for an arbitrary number of bubbles. The Green's function takes into account the boundary conditions associated with interfaces between the liquid and confining interfaces and between different layers of a microfluidic device. Because it is a solution of the linear equations of motion, the Green's function requires that the stresses and strains induced in the viscoelastic layers by the bubble dynamics be relatively small. Since the simulations in this paper are for channels with hard walls, this requirement is satisfied. In addition, the model described here only accounts for spherical pulsation of the bubbles.

Here we present a model for the coupled dynamics of two pulsating bubbles positioned in the centre of a channel formed by two identical nearly rigid layers. This is a modification of the model described by Hay *et al.* (2012), which describes the pulsation of a single bubble between two arbitrary viscoelastic layers. The two layers bounding the bubble are assumed to be infinite in the x, y-plane but have finite thickness h_l along the z-axis. The layers have density ρ_l, dilatational viscosity ζ_l, shear viscosity η_l, Lamé parameter λ_l, and shear modulus μ_l, while the liquid surrounding the layers has density ρ, sound speed c, Lamé parameter $\lambda = \rho c^2$, dilational viscosity ζ and shear viscosity η (see figure 1).

Liquid compressibility, leading to the loss of energy due to acoustic radiation, and viscous forces, including viscous stresses acting along the layer interfaces, are fully taken into account in this model. Inclusion of viscous losses is particularly important in the present case because, as discussed by Hay *et al.* (2012), it decreases the pulsation amplitude significantly if a harmonically driven bubble is positioned less than $\sim 5R_0$ from an interface. The rapid decrease in bubble pulsation amplitude near a boundary has been confirmed by experiments (Overvelde *et al.* 2007). In addition, acoustic radiation is the dominant loss mechanism in the pulsation of cylindrical bubbles with radius greater than 1 μm (Ilinskii *et al.* 2012). While only spherical

https://doi.org/10.1017/jfm.2012.526 Published online by Cambridge University Press

bubbles are considered in this section, the two-dimensional nature of the flow field far from the bubble in narrow channels results in a dynamical response similar to that for cylindrical bubbles.

The Green's function is derived by considering the momentum equation for an isotropic viscoelastic medium:

$$\left(\lambda + \zeta\frac{\partial}{\partial t} + \mu + \eta\frac{\partial}{\partial t}\right)\boldsymbol{\nabla\nabla}\cdot\boldsymbol{u} + \left(\mu + \eta\frac{\partial}{\partial t}\right)\nabla^2\boldsymbol{u} = \rho\frac{\partial^2\boldsymbol{u}}{\partial t^2} \tag{3.30}$$

where t is time, and $\boldsymbol{u}$ is displacement. The Green's function g_j for displacement due to a volume point source located at r_j and pulsating with time dependence $\mathrm{e}^{-\mathrm{i}\omega t}$ satisfies

$$(\hat{\lambda} + \hat{\mu})\boldsymbol{\nabla\nabla}\cdot g_j + \hat{\mu}\nabla^2 g_j = s\boldsymbol{\nabla}\delta(r - r_j), \tag{3.31}$$

in the liquid between the elastic layers. In (3.31) δ is the Dirac delta function, $\widehat{\lambda} = \lambda - \mathrm{i}\omega\zeta$ and $\hat{\mu} = \mu - \mathrm{i}\omega\eta$ are complex Lamé parameters, where $\lambda = \rho c^2$, c is the sound speed, and s is the source strength which, as discussed by Mitragotri (2005), is related to the volume velocity Q of the source as $s = -(\rho c^2/\mathrm{i}w)Q$. For the present geometry with two interacting bubbles the total displacement is given by $g = g_1 + g_2$.

Within the viscoelastic layers the Green's function satisfies

$$(\hat{\lambda}_l + \hat{\mu}_l)\boldsymbol{\nabla\nabla}\cdot g + \hat{\mu}_l\nabla^2 g + \rho_l\omega^2 g = 0, \tag{3.32}$$

where $\hat{\lambda}_l = \lambda_l - \mathrm{i}\omega\zeta_l$ and $\hat{\mu}_l = \mu_l - \mathrm{i}\omega\eta_l$ are complex Lamé parameters. Equations (3.31) and (3.32) are coupled by boundary conditions (continuity of displacement and stress) at the interfaces. In order to satisfy the boundary conditions the Green's function is decomposed into its angular spectrum in planes parallel to the layers. Once the angular spectrum of the Green's function is found (see Hay *et al.* 2012 for a complete derivation) the frequency response of the channel with a source located at r_i and a receiver located at r_j may be expressed in terms of the inverse Fourier transform

$$H_{ij}(\omega, D_{ij}) = R_{0i}\int_0^\infty \tilde{\Psi}_{rev}(\kappa)\mathrm{J}_0(\kappa D_{ij})\frac{\kappa}{\kappa_l}\,\mathrm{d}\kappa, \tag{3.33}$$

of the displacement potential $\widetilde{\Psi}_{rev}$ with respect to wavenumber κ, where $D_{ij} = |r_i - r_j|$, J_0 is the zeroth-order Bessel function of the first kind, κ_l is the component of the wave vector along the z-axis corresponding to longitudinal waves, and R_{0i} is the equilibrium radius of the ith bubble. The integration indicated in (3.33) must be performed numerically. For $i = j$, (3.33) gives the frequency response of the reverberant pressure experienced by bubble i due to its own motion and for $i \neq j$ it gives the frequency response due to the adjacent bubble.

The total reverberant pressure in the channel at the location of bubble i is

$$P_{rev_i}(\omega, D_{bub}) = P_{free_i}(\omega)H_{ii}(\omega, 0) + P_{free_j}(\omega)H_{ji}(\omega, D_{bub}), \tag{3.34}$$

where $P_{free_i}(\omega)$ and $P_{free_j}(\omega)$ are the pressures radiated by the bubbles in a free field. With the reverberant pressure calculated, the dynamical equation describing the time-dependent radius R_i of the ith bubble may be written

$$R_i\ddot{R}_i + \frac{3}{2}\dot{R}_i^{\,2} = \frac{P_i - P_{rev_i}}{\rho} - \frac{R_j}{H_{gap}}(R_j\ddot{R}_j + 2\dot{R}_j^2), \tag{3.35}$$

https://doi.org/10.1017/jfm.2012.526 Published online by Cambridge University Press

where $j = 2$ if $i = 1$ or $j = 1$ if $i = 2$, overdots denote derivatives with respect to time,

$$P_i = \left(P_{amb} + \frac{2\sigma}{R_{0i}}\right)\left(\frac{R_{0i}}{R_i}\right)^{3\kappa} + P_v - \frac{2\sigma}{R_i} - \frac{4\eta\dot{R}_i}{R_i^2} - P_{amb} - P_{ac}(t), \tag{3.36}$$

where $P_{ac}(t)$ is an imposed acoustic pressure, and $P_{\mathrm{rev}\,i}$ is the inverse Fourier transform of (3.34), i.e.

$$P_{rev_i} = \rho\left[\frac{R_i}{R_{0i}}(R_i\ddot{R}_i + 2\dot{R}_i^2) * h_{ii}(t) + \frac{R_j}{R_{0j}}(R_j\ddot{R}_j + 2\dot{R}_j^2) * h_{ji}(t)\right]. \tag{3.37}$$

In (3.37) h_{ii} and h_{ji} are inverse Fourier transforms of the quantities H_{ii} and H_{ji} calculated from (3.34).

The last term in (3.35) corresponds to the pressure transmitted along the direct path between the two bubbles, whereas the two convolutions in (3.37) correspond to the reverberant pressure field. All terms in (3.35) are therefore independent of the layers, while the reverberant pressure in (3.37) vanishes in the absence of the layers.

3.2.2. *Derivation of the maximum bubble volume*

Finally, for both the boundary element model described in § 3.1 and the mathematical model described in the present section, a useful benchmark is provided by an equation for the maximum volume attained by a bubble that is released from rest in an initially pressurized state. Obtained on the basis of energy conservation (Ilinskii *et al.* 2012), the result is applicable to arbitrary plate geometries constraining the flow around the bubble (i.e. they may be circular, rectangular, etc.) provided the plates are rigid, and losses are negligible (viscous, thermal, and radiation). The bubble, which need not be spherical, is assumed to be momentarily at rest in its initial and final states and therefore the only changes are in the potential energy associated with surface tension. The result is

$$\frac{1}{k-1}(P_{g_0}V_0 - P_{g1}V_1) + (P_v - P_{amb})(V_1 - V_0) = S_1 - S_0, \tag{3.38}$$

where indices 0 and 1 indicate initial and final states, respectively, and S is the energy stored in surface tension. This result is not restricted to small bubble wall displacements.

In addition to the neglect of viscosity, another approximation is that at maximum volume the bubble wall is momentarily at rest, even though results from the BEM indicate that this is not exactly the case. Nevertheless, comparisons of predictions based on (3.38) with measurements of non-spherical bubble growth by Gonzalez-Avila *et al.* (2011) fall within the reported experimental error.

For a spherical bubble the gas law is given by (3.19), the surface energy by $S = 4\pi R^2\sigma$, and (3.38) can be written in the form (Ilinskii *et al.* 2012)

$$(P_{amb} - P_v)(x^3 - 1) + \frac{3\sigma}{R_0}(x^2 - 1) - \frac{P_{g0}}{\kappa - 1}[1 - x^{-3(\kappa-1)}] = 0, \tag{3.39}$$

which can be solved numerically for the dimensionless maximum radius $x = R_1/R_0$ as a function of the initial radius R_0 and gas pressure P_{g_0}. Equation (3.39) is seen to be an alternative form of (3.16). The difference here is the starting point, as (3.39) is not restricted to spherical bubbles. For example, if the bubble is not spherical in its final state, then (3.39) still applies except that R_1 is then interpreted as the radius of a sphere having the same volume V_1, such that $R_1 = (3V_1/4\pi)^{1/3}$. Here we only draw attention to the fact that for bubble growth between parallel circular disks as

https://doi.org/10.1017/jfm.2012.526 Published online by Cambridge University Press

considered in the present work, under the ideal conditions (no losses) leading to (3.39), and provided the effect of surface tension at maximum volume is relatively weak, the maximum bubble radius is independent of both the diameters of the plates and the separation distance between them. Increasing the plate diameters or decreasing the separation distance merely increases the time until the bubble achieves its maximum radius, the time increase being due to the increased intertance of the liquid resulting from the more restricted flow in the channel.

An equation similar to (3.39) can be obtained for a cylindrical bubble between parallel plates with separation distance or channel height H_{gap} by using the relation $P_g R^{2k} = \text{constant}$ in place of (3.12) for the gas law, and $S = 2\pi R H_{gap}\sigma$ for the surface energy. The latter expression accounts for energy stored in tension only at the cylindrical surface of the bubble, and not at the circular plane surfaces in contact with the plates. The approximation is reasonable if at the ends of the bubble the gas is in direct contact with the plates. If a liquid layer separates the gas from the plates then the surface tension at these interfaces may be important.

Especially relevant to experiments with laser-generated bubbles between parallel plates is the evolution of a bubble that starts spherical in its initial compressed state and expands sufficiently to become cylindrical in its final state. Equation (3.39) may be applied to this case as well, with the quantities for the initial state evaluated for a spherical bubble, and those for the final state evaluated for a cylindrical bubble. Doing so, and ignoring surface tension where the bubble wall is in contact with the plates, yields in place of (3.39) (Ilinskii *et al.* 2012)

$$(P_{amb} - P_v)\left(\frac{3a}{2}x^2 - 1\right) + \frac{3\sigma}{R_0}(ax - 1) - \frac{P_{g0}}{k-1}\left[1 - \left(\frac{2}{3a}\right)^{k-1} x^{-2(k-1)}\right] = 0, \quad (3.40)$$

where $a = D_{gap}/2R_0$, such that $a = 1$ corresponds to a spherical bubble of initial volume $V_0 = (4/3)\pi R_0^3$ that just touches the disks, and again $x = R_1/R_0$, but here R_1 is the final (maximum) radius of a cylindrical bubble of volume $V_1 = \pi R_1^2 H_{gap}$.

Solutions of (3.39) and (3.40) are discussed in § 4.

4. Results and discussion

4.1. *Single-bubble dynamics between two disks*

In the first part of this study, the dynamics of a single bubble between two rigid circular disks is simulated with both models in order to elucidate the effect of the basic parameters in the simulation on the bubble dynamics. Key parameters in the dynamics are: (i) the physical properties of the liquid: density ρ, kinematic viscosity υ, vapour pressure p_v; (ii) the liquid/bubble interface property: surface tension parameter σ; and (iii) the imposed pressure conditions: liquid initial ambient pressure P_{amb}, and initial bubble gas content pressure P_{g0}. In addition, the gap between the two plates, H_{gap}, and the radius of each disk, R_{disk}, are important parameters to consider.

For the single-bubble dynamics studies the following physical parameters will be maintained constant:

(i) liquid density $\rho = 10^3$ kg m^{-3};
(ii) kinematic viscosity $\upsilon = 10^{-6}$ m^2 s^{-1};
(iii) ambient pressure $P_{amb} = 101\,235$ Pa;
(iv) vapour pressure $P_v = 2300$ Pa;
(v) surface tension $\sigma = 0.07275$ N m^{-1};
(vi) initial bubble radius $R_0 = 2$ μm.

https://doi.org/10.1017/jfm.2012.526 Published online by Cambridge University Press

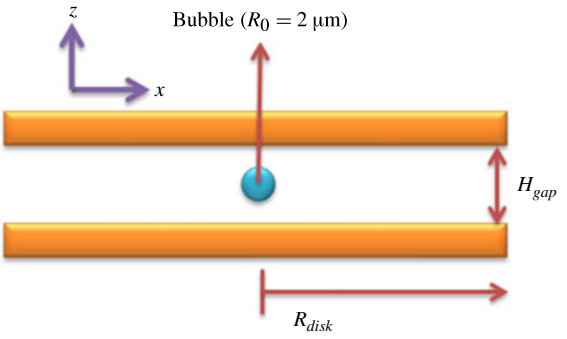


FIGURE 2. (Colour online) Setup used for numerical simulations of a single bubble between circular disks.

In addition, the following parameters must be specified for the mathematical model described in § 3.2:

(i) sound speed in liquid $c = 1484$ m s^{-1};

(ii) layer density $\rho_t = 2300$ kg m^{-3};

(iii) layer Lamé parameters $\lambda = 64$ GPa and $\mu = 27$ GPa;

(iv) layer thickness $h_1 = 1$ cm.

The parameters for the layers correspond to those of stainless steel. For simplicity the shear and dilatational viscosities in the layers were neglected.

The gap between the disks, H_{gap}, was chosen to be 2 μm to correspond to one of the gap sizes used in a set of actual experiments. Unfortunately, experimental results are not available yet for most of the systematic simulations shown below. Figure 2 shows the setup used for the numerical simulations.

In order to compare the methods of solution under extreme bubble dynamics behaviours, two different dynamic conditions are considered based on the imposed initial non-equilibrium internal bubble pressure conditions imposed. The first corresponds to small-amplitude oscillations while the other corresponds to the large-amplitude oscillations of a bubble between two disks, corresponding to the Duke experiments on laser-induced optical breakdown between two plates.

4.1.1. *Maximum single-bubble radius*

Figure 3 compares the time history of equivalent spherical bubble radius, R_{eq}, obtained from the BEM model computations for unbounded growth of a single bubble (dashed lines) with constrained bubble growth between disks separated by distance $H_{gap} = 25$ μm(solid lines with symbols) for $R_0 = 2$ μm and three values of P_{g0}. At any given time, the equivalent radius, R_{eq}, is the radius of a spherical bubble having volume equal to the volume of the bubble under consideration. Since the maximum bubble diameter in all cases is considerably less than H_{gap}, the bubble shape remains approximately spherical, and (3.40) applies. Consistent with (3.40), it is seen that including the disks does not affect the maximum equivalent bubble radius, R_{max}; it merely increases the time the bubble takes to reach its maximum radius. For the initial gas pressures $P_{g0} = 2$, 5 and 10 atm used in the simulations, R_{max} is seen in figure 3 to be 2.2, 3.4 and 4.6 μm, respectively.

https://doi.org/10.1017/jfm.2012.526 Published online by Cambridge University Press

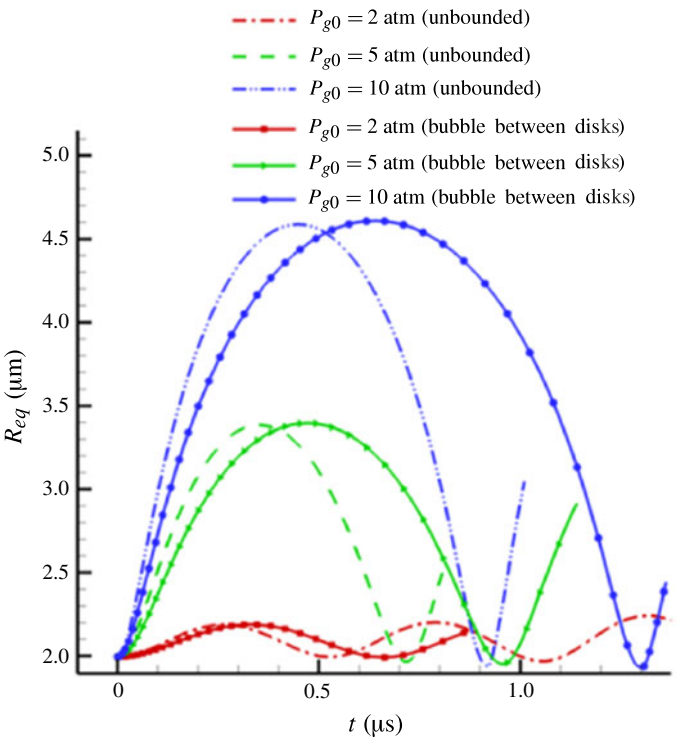


FIGURE 3. (Colour online) Bubble equivalent radius versus time calculated with 3DYNAFS© for three different gas pressures, P_{g0}, for unbounded and bounded single-bubble oscillations: $H_{gap} = 25$ μm, $R_0 = 2$ μm. The radius of the disk used in the 3DYNAFS© computations was $R_{disk} = 750$ μm.

Comparison of (3.40) with BEM model computations for a bubble that grows between disks to become cylindrical in shape follows the discussion of figures 10–12 below, and agreement is again found to be excellent.

4.1.2. *Small-amplitude oscillations*

First, comparison is made between the two models for small-amplitude oscillations of a single bubble between two parallel disks. Three different initial bubble gas pressures (driving pressures), P_{g0}, are presented below. To ensure that the two models are accounting in the same way for the physical quantities considered, we compare first the results of the two models for one of the three cases, $P_{g0} = 10$ atm, which corresponds to the largest oscillations considered in this section. Figure 4 shows the comparison of bubble radius versus time under the same conditions for the bubble in the absence of the two disks (unbounded medium) as well as between two parallel disks. It is seen that in the unbounded case comparison of the radius versus time for the period of interest here (the first cycle) is quite good with the differences being mainly due to numerical errors from the discretization in 3DYNAFS-BEM© (i.e. increasing the grid number reduces the differences) and due to the neglected compressibility effects. In these computations the bubble surface was discretized with 1026 nodes and 2048 panels. Better results can be obtained with a finer discretization but at an increased CPU cost.

https://doi.org/10.1017/jfm.2012.526 Published online by Cambridge University Press

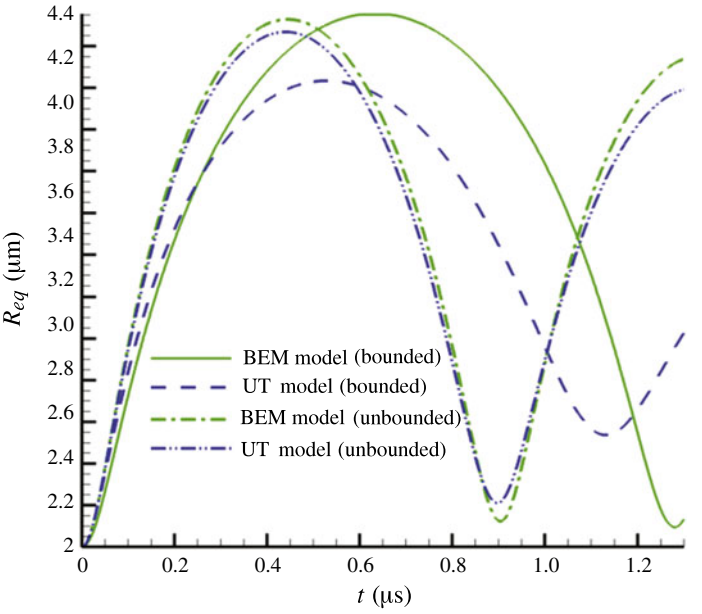


FIGURE 4. (Colour online) Comparison of bubble radius versus time between 3DYNAFS-BEM© and the UT model for small-amplitude oscillations of a single bubble in an unbounded medium and between two parallel disks ($H_{gap} = 25$ μm, $R_0 = 2$ μm, $P_{g0} = 10$ atm, $R_{disk} = 750$ μm).

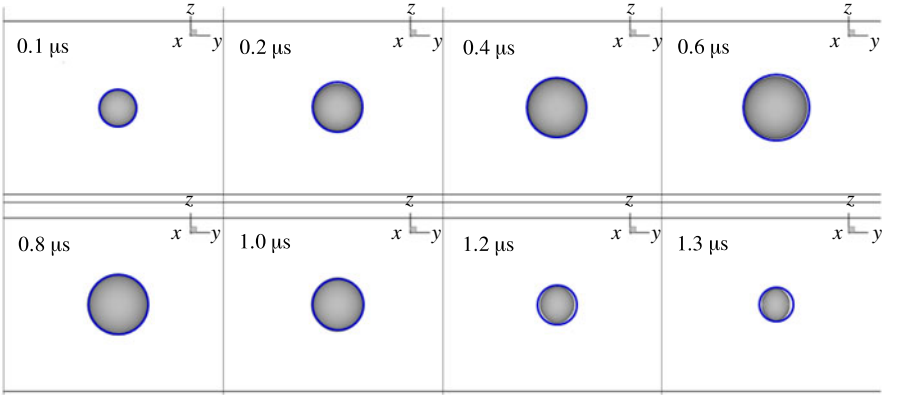


FIGURE 5. (Colour online) Side view of the bubble contours between the two disks obtained with 3DYNAFS-BEM©, showing small deviations from the spherical shape ($H_{gap} = 25$ μm, $R_0 = 2$ μm, $P_{g0} = 10$ atm, $R_{disk} = 750$ μm). A circle around the bubble is added to illustrate its deviation from sphericity.

Figure 4 also illustrates the effect of the presence of the two boundaries on the bubble dynamics. Note that in this case the maximum bubble diameter is ∼9 μm, while the plate spacing is 25 μm; this corresponds to the limit of weak interaction between a bubble and a wall. The bubble shape and its deviation from a sphere during the first oscillation is shown in figure 5. We can see that the bubble slightly deviates

https://doi.org/10.1017/jfm.2012.526 Published online by Cambridge University Press

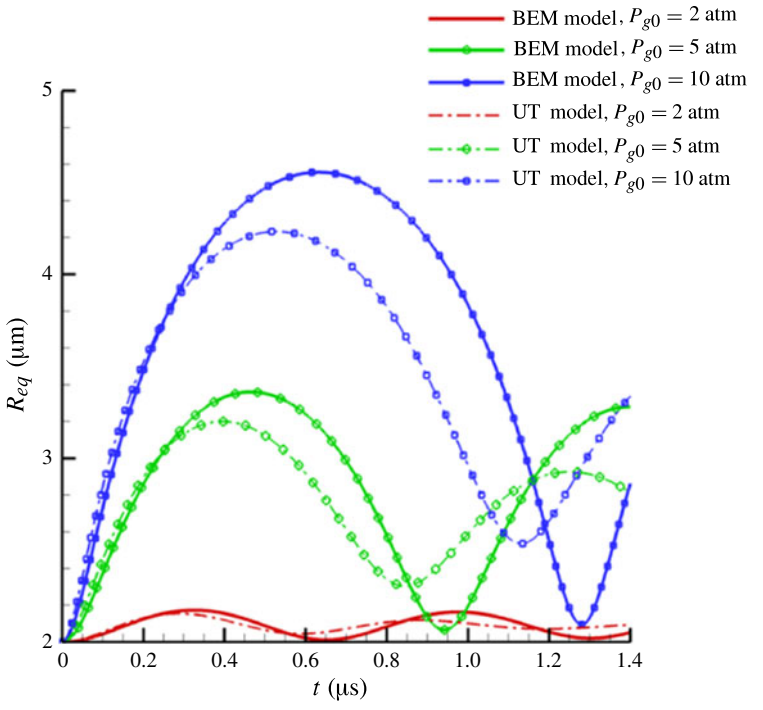


FIGURE 6. (Colour online) Equivalent radius versus time for small-amplitude oscillations of a single bubble between two parallel plates. Comparisons between 3DYNAFS-BEM© and UT model for the three initial gas pressures: $P_{g0} = 2$, 5 and 10 atm. ($H_{gap} = 25$ μm, $R_0 = 2$ μm, $R_{disk} = 750$ μm.)

from the spherical shape, mainly towards the end of the cycle and tends to deform as an oval shape with its long axis normal to the disk surface. The confinement increases the bubble period but its effect on the bubble maximum radius is not captured in the same way between the two approaches. While 3DYNAFS-BEM© detects practically no influence on the maximum value of the radius, in agreement with (3.40), the UT model including liquid compressibility and the viscous boundary layer along the walls detects a significant reduction of R_{max} (∼7 % in this case) due to acoustic energy losses. For the same reason, the bubble period is smaller than with the incompressible code (by ∼15 % in this case), even though it is significantly larger than in the case of an infinite medium (by ∼25 % in this case). The bubble minimum radius at the end of the first period is also larger with the UT model (∼$1.3R_0$ in this case); while it is $1.05R_0$ with 3DYNAFS-BEM©, where the only losses considered are viscous losses. The 3DYNAFS-BEM© code will be improved in future versions to account for the compressible acoustic losses brought out in this study.

Figure 6 shows the equivalent bubble radius versus time as obtained from 3DYNAFS-BEM© and the UT model for the three initial gas pressures, P_{g0}, considered. It can be seen from the plots that, as expected, the deviations between 3DYNAFS-BEM© and the UT model reduce significantly as the bubble oscillations and the effects of the walls are reduced.The two results asymptotically approach each other and the per cent difference in R_{max}, ϵ, due to these effects reduces from 7.1 % to 0.8 % as the driving amplitude, P_{g0}, is decreased from 10 atm to 2 atm as shown

https://doi.org/10.1017/jfm.2012.526 Published online by Cambridge University Press

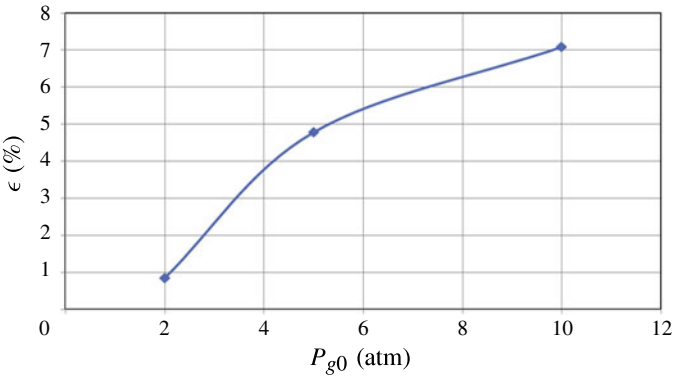


FIGURE 7. (Colour online) Percentage difference in the values of R_{max} between 3DYNAFS-BEM© and the UT model for different driving pressures, P_{g0}.

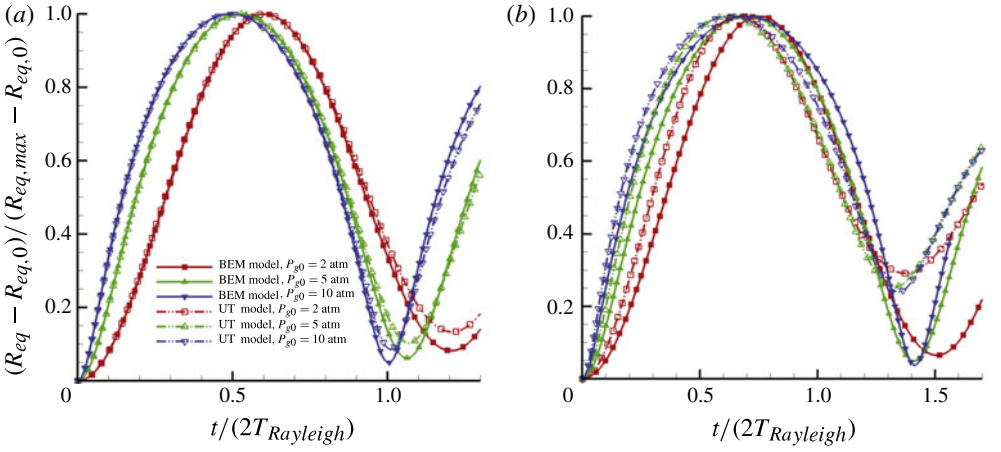


FIGURE 8. (Colour online) Normalized equivalent radius versus normalized time for small bubble oscillations. Comparisons between 3DYNAFS-BEM© and the UT model for three initial gas pressures ($P_{g0} = 2$ atm, 5 atm and 10 atm). (*a*) Unbounded bubble, (*b*) bubble between plates.

in figure 7. Again, the UT model with compressibility and viscous boundary layers taken into account predicts a lower maximum equivalent bubble radius, R_{max}, a smaller period for the same initial gas pressure in the bubble, P_{g0}, and a larger minimum bubble radius at the end of the first period. The presence of the disks and the decrease of the ratio $2R_{max}/H_{gap}$ appear to increase the non-spherical deformations and the losses.

Figure 8 shows normalized plots of bubble equivalent radius versus time for the same conditions as in figure 6. Time is normalized by the classical Rayleigh time defined as

$$T_{Rayleigh} = 0.915 R_{max} \sqrt{\frac{\rho}{p_{amb}}}. \tag{4.1}$$

https://doi.org/10.1017/jfm.2012.526 Published online by Cambridge University Press

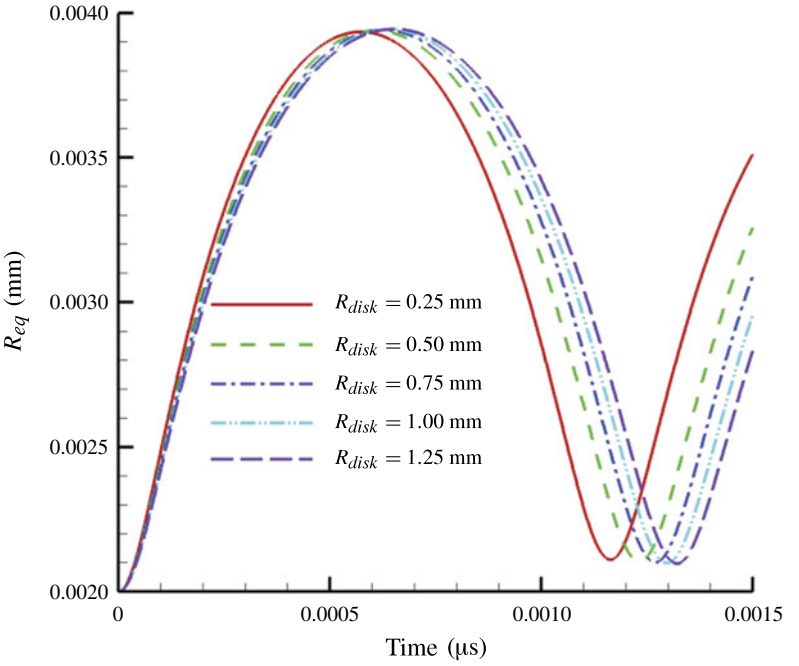


FIGURE 9. (Colour online) Bubble equivalent radius versus time for five different disk sizes, R_{disk}, for small-amplitude bubble oscillations: $H_{gap} = 25.0$ μm, $R_0 = 2$ μm, $R_{max} = 3.3$ μm.

In order to compare all cases properly, the bubble equivalent radii are normalized as follows:

$$\bar{R} = \frac{R_{eq}(t) - R_{eq}(0)}{R_{max} - R_{eq}(0)}, \quad R_{eq}(0) = R_0. \tag{4.2}$$

From the normalized plot, it can be seen that the two models match perfectly for the unbounded case whereas for the bounded case the BEM model predicts a longer period.

4.1.3. *Effect of disk size*

Besides the liquid compressibility and viscous boundary layers, another important difference between 3DYNAFS-BEM© and the UT model is that the 3DYNAFS-BEM© takes into account the finiteness of the disk size. This is important because as the bubble dynamics evolves, the pressure around the bubble is very significantly affected by the presence of the two disks. From simple consideration of the Bernoulli equation, for the same bubble volume change rate the flow velocity in the radial direction, u_r, will be larger when two plates confine the bubble dynamics than when the bubble is in an infinite medium, and this effect will become more significant as the ratio $R_{eq}(t)/H_{gap}$ increases. Confinement transforms the three-dimensional flow to two dimensions. This results in increasing locally the liquid velocity at a given radial distance from the bubble centre. This in turn lowers the pressures around the bubble and thus increases the bubble period. This effect can be seen in figure 9, which shows a prolonged bubble period as a result of increased disk radius. The maximum bubble radius is, however, unaffected, as expected from energy considerations (recall (3.40)).

https://doi.org/10.1017/jfm.2012.526 Published online by Cambridge University Press

An asymptotic theory can be derived in the limiting cases where the bubble size approaches the inter-plate gap and/or when the plate diameter is much larger than the bubble maximum diameter. In those cases, a two-dimensional cylindrical flow field can be derived. For a small gap for example, the leading-order solution of the problem becomes the behaviour of a two-dimensional bubble, for which the velocity potential solution can be written as

$$\phi(r,t) = R\dot{R}\log(r), \tag{4.3}$$

where r is the radial cylindrical coordinate and R the bubble radius.

The logarithmic singularity in $\partial\phi/\partial n$ at infinity makes it impossible to impose a quiescent far-field condition with a given reference pressure if the disk extends to infinity. For a finite disk radius, R_D, the Bernoulli equation can be written relating an arbitrary location, r, and the disk edge, where the pressure can be imposed. This leads to

$$\frac{p(r,t)}{\rho} + \frac{1}{2}\left\{\left(\frac{R\dot{R}}{r}\right)^2 - \left(\frac{R\dot{R}}{R_D}\right)^2\right\} + \log\left(\frac{r}{R_D}\right)[R\ddot{R} + \dot{R}^2] = \frac{p_\infty(t)}{\rho}. \tag{4.4}$$

This expression illustrates that the bubble dynamics depends on the disk size, R_D. Normalization leads to a characteristic bubble period, which is given by the Rayleigh time multiplied by parameter $\{\log(R_D/R_{max})\}^{1/2}$,

$$T_{asymp} = 0.915R_{max}\sqrt{\log\left(\frac{R_D}{R_{max}}\right)\frac{\rho}{p_{amb}}}. \tag{4.5}$$

This again illustrates that the period increases with the disk size as more liquid inertia needs to be overcome as R_D increases.

4.1.4. *Large-amplitude oscillations*

Next, we consider single-bubble dynamics cases between two parallel disks where P_{g0}/P_{amb} is much large than one. This is a different family of behaviours since the high potential energy in the bubble results in large bubble growth, i.e. in $R_{max}/R_0 \gg 1$, which also results here in $2R_{max}/H_{gap}$ on the order of or larger than 1. This corresponds for instance to the laser-generated bubbles in the Duke experiments reported in Sankin *et al.* (2010). The bubble in this case actually transitions from a quasi-spherical shape to a quasi-cylindrical shape during its oscillation cycle as its equivalent diameter approaches or exceeds the gap size between the two disks. For a numerical code using discretized boundaries, this type of large-amplitude bubble oscillation imposes strong gridding constraints on the relative sizes of the grids on the bubbles and on the plates, as well as on the relative sizes of the grids and the local distances between the approaching surfaces.

The numerical results in this case will be verified against available experimental results by Sankin *et al.* (2010). Since, in this case, the initiation of the bubble is due to high-energy laser deposition and liquid vaporization, the physics of which is not considered in this study, the dynamics can be modelled, as for underwater explosions (Chahine *et al.* 1989; Chahine & Duraiswami 1993; Chahine 2005), by the selection of fictitious or idealized initial boundary conditions parameters, R_0 and P_{g0}, which results in the correct value of R_{max} when the laser discharge occurs in the unconfined medium.

In the absence of unbounded-field experimental data, the bubble characteristics from the bounded-field experiments were matched directly to determine R_0 and P_{g0}. The maximum value of the projected bubble radius, R_{proj} (corresponding to

https://doi.org/10.1017/jfm.2012.526 Published online by Cambridge University Press

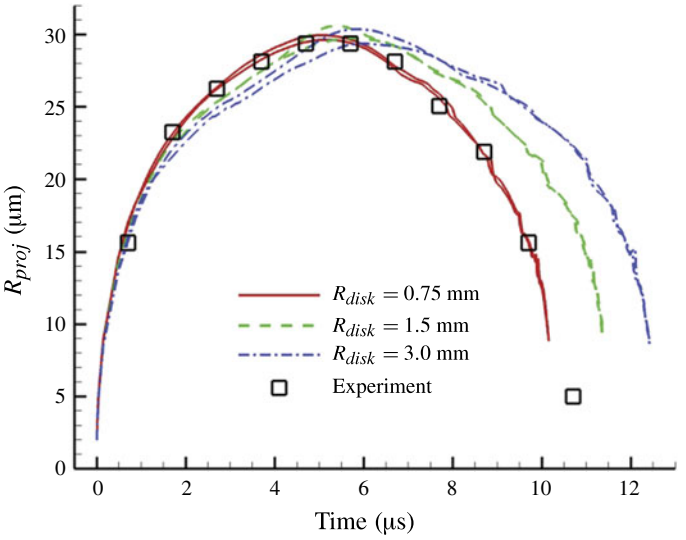


FIGURE 10. (Colour online) Radius of projected area of the bubble versus time: comparison of experimental results from Sankin *et al.* (2010) with BEM model with parameters $H_{gap} =$ 25.0 μm, $R_{disk} = 0.75$ mm, 1.5 and 3.0 mm, $R_{max} = 24.5$ μm, $R_0 = 2$ μm and $P_{g0} = 835$ atm.

the experimentally observed top view of the bubble through the upper transparent disk), was used here. Practically, P_{g0} was first iterated using a fixed $R_0 = 2$ μm and a guessed R_{disk} until R_{proj} was matched. As shown in figure 9, the disk size only influences the bubble period but not the value of R_{max} (as well as R_{proj} as shown in figure 10). Therefore, the assumed disk radius is not important when R_0 and P_{g0} are determined by matching R_{proj}. However, R_{disk}, the radius of the two idealized disks in the numerical study, affects the bubble period and was selected to match the period of the single bubble from the experimental measurement. The same initial conditions and plate size are then used for all test conditions including for tandem bubbles and are not adjusted from case to case.

Such a 'fitting' obviously results in matching two points on the $R_{proj}(t)$ curve; however, the measure of acceptance of the numerical method is how well the numerical results match all other points on the $R_{proj}(t)$ curve, as well as how well the results match for the full three-dimensional shapes. In addition, once a fit for R_0 and P_{g0} is found, the same initial parameters are used for the tandem bubbles or for the different values of H_{gap}, and then the numerical code is judged by how good of a match is obtained under these conditions.

As shown in figure 10, for the laser-generated single bubble between plates the results obtained with 3DYNAFS-BEM© with $R_0 = 2$μm, $P_{g0} = 835$ atm, $H_{gap} = 25$ μm and $R_{disk} = 0.75$ mm were found to give the best match with the experimental results. With this condition, the maximum bubble equivalent radius, R_{max}, reached 24.5 μm. As we can also see in the figure for illustration, increasing R_{disk} to 1.5 and 3 mm results in significant increases of the bubble period and very strong deviation from the experimental results.

Figure 11 shows the projected view of the bubble in the middle plane obtained both from the experiments in Sankin *et al.* (2010) and from the 3DYNAFS-BEM© simulations. The computations show a very good correspondence between

https://doi.org/10.1017/jfm.2012.526 Published online by Cambridge University Press

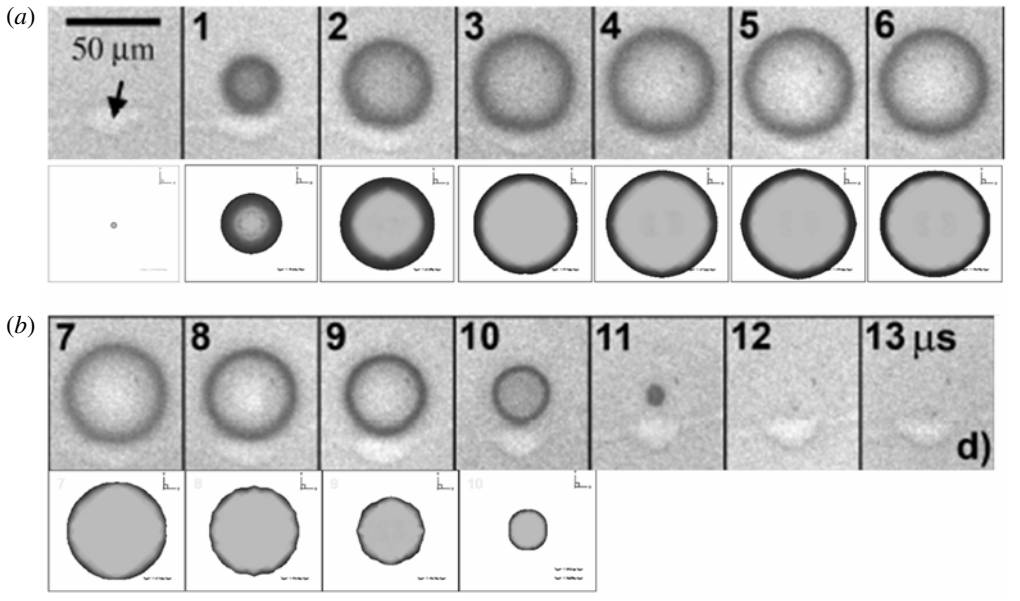


FIGURE 11. Projected view of the bubble: (*a*) experiments from Sankin *et al.* (2010) and (*b*) 3DYNAFS-BEM© simulations, from 1 to 13 μs at intervals of 1 μs l. Numerical conditions: $H_{gap} = 25.0$ μm, $R_{disk} = 0.75$ mm, $R_{max} = 24.5$ μm, $R_0 = 2$ μm and $P_{g0} = 835$ atm.

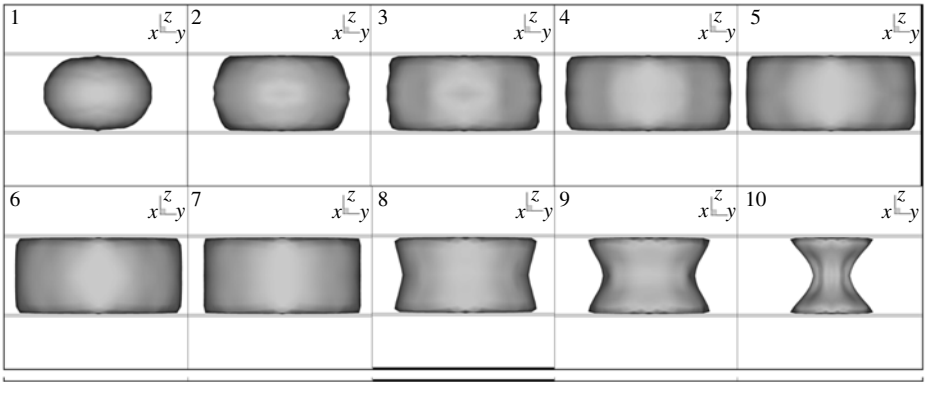


FIGURE 12. Side view of the bubble dynamics between two disks from the 3DYNAFS-BEM© numerical simulations from 1 to 10 μs at intervals of 1 μs. Numerical conditions: $H_{gap} = 25.0$ μm, $R_{disk} = 0.75$ mm, $R_{max} = 24.5$ μm, $R_0 = 2$ μm and $P_{g0} = 835$ atm.

the sizes and the timing of the various sequences. Figure 12 shows side profiles of the bubble with confining disks at the top and bottom as obtained from the same 3DYNAFS-BEM© numerical simulations. This view was not recorded in the experiments by Sankin *et al.* (2010). However, the same qualitative trend has been obtained for various ratios of R_{max}/H_{gap} in our earlier studies summarized in Chahine & Morine (1980), Darrozes & Chahine (1983) and Chahine (1991). It can be seen that during the growth phase the presence of the two boundaries causes the bubble

https://doi.org/10.1017/jfm.2012.526 Published online by Cambridge University Press

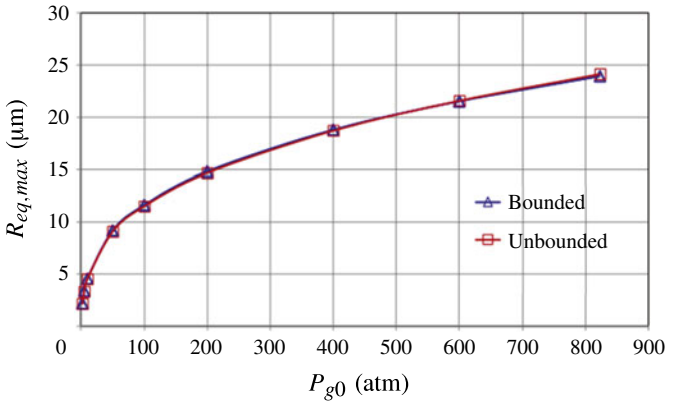


FIGURE 13. (Colour online) Comparison of R_{max} between bounded and unbounded cases at different driving pressures, P_{g0} ($H_{gap} = 25.0$ μm, $R_{disk} = 0.75$ mm, $R_0 = 2$ μm).

to flatten and grow as a pancake, thus turning into a cylindrical shape. As the bubble starts to collapse, the central region between the two plates collapses faster resulting in an hourglass shape. This behaviour accelerates until the bubble splits into two in the centreplane between the two disks.

As shown in figure 12, the bubble shape at maximum volume is cylindrical, and therefore (3.40) is applicable. For this case, in which $P_{g0} = 835$ atm, (3.40) yields $R^{cyl}_{max} = 29$ μm, in excellent agreement with the maximum values of R_{proj} observed in figure 10.

4.1.5. *Effect of wall confinement on bubble dynamics*

To better illustrate the effect of wall confinement on the bubble dynamics, R_{max} and bubble period, $T_{collapse}$, obtained from both unbounded and bounded domains are compared for different driving pressure P_{g0}. It can be seen from figure 13 that the wall confinement does not have any significant effect on the maximum bubble size. The difference in surface tension energy between a spherical bubble (unbounded) and a cylindrical bubble (bounded) is expected to generate a slightly smaller maximum volume for the cylindrical one when all energy is potential. For the spherical unbounded bubble the total energy is completely converted to potential energy, $(3/4)\pi R^3_{max}(P_{amb} - P_g)$, when the bubble reaches R_{max}. However, this is not exactly the case for the bounded bubble, as some kinetic energy remains at maximum volume due to the non-spherical dynamics and phasing of the motion between different points on the bubble surface. In addition, for the cases of concern here, the pressure due to the surface tension is very small compared to P_{g0}, resulting in a minor influence of the surface tension.

On the other hand, as discussed earlier, wall confinement has a significant effect on the bubble period. Figure 14 shows the comparison of the bubble period ($T_{collapse}$) between bounded and unbounded cases at different P_{g0}. It is seen that as P_{g0} increases, the difference between bounded and unbounded cases increases. Since increasing P_{g0} results in higher ratios R_{max}/H_{gap}, the behaviour of the bubble becomes closer to a two-dimensional cylindrical one and expression (4.5) applies.

https://doi.org/10.1017/jfm.2012.526 Published online by Cambridge University Press

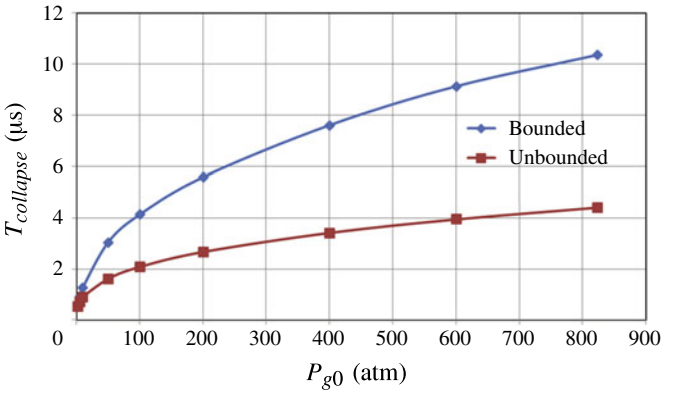


FIGURE 14. (Colour online) Comparison of bubble period between bounded and unbounded cases at different driving pressures, P_{g0} ($H_{gap} = 25.0$ μm, $R_{disk} = 0.75$ mm, $R_0 = 2$ μm).

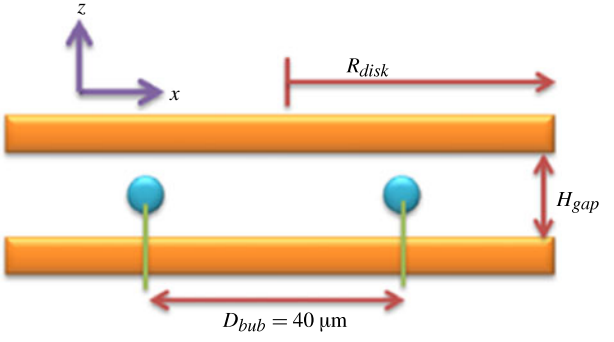


FIGURE 15. (Colour online) Set-up used for numerical simulations of tandem bubbles.

4.2. *Tandem-bubble dynamics between two disks*

The numerical models presented earlier were also applied for the simulation of the tandem bubbles used in the studies presented in Sankin *et al.* (2010). As in the experiments the spacing between the two bubbles was 40 μm and $H_{gap} = 25$ μm (see figure 15). The initial conditions for each of the tandem bubbles and the disk size were chosen to be those that best match the experimental results in the single-bubble case, i.e. $R_0 = 2$ μm, $P_{g0} = 886$ atm and $R_{disk} = 0.75$ mm.

4.2.1. *Small bubble oscillations*

As in the single-bubble cases, before proceeding with simulations of large-amplitude oscillations of tandem bubbles, their small oscillations were studied using 3DYNAFS-BEM© and the UT model. These simulations were performed with the two tandem bubbles oscillating in synchrony, i.e. expanding and collapsing simultaneously. Figure 16 shows the equivalent bubble radius of one of the tandem bubbles versus time obtained from 3DYNAFS-BEM© and the UT model for three different relatively small driving pressures, P_{g0}. As was observed for the small-oscillation cases for a single bubble between two disks, the UT model predicts a maximum bubble radius that is smaller than that predicted by 3DYNAFS-BEM©. This is attributed to energy

https://doi.org/10.1017/jfm.2012.526 Published online by Cambridge University Press

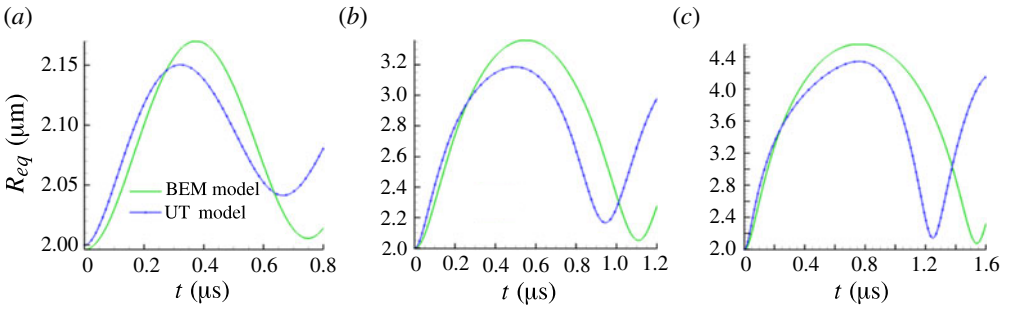


FIGURE 16. (Colour online) Comparison between 3DYNAFS-BEM© and the UT model of the equivalent radius versus time for small bubble in the case of tandem bubbles subjected to smaller oscillations: (*a*) $P_{g0} = 2$ atm; (*b*) $P_{g0} = 5$ atm; (*c*) $P_{g0} = 10$ atm.

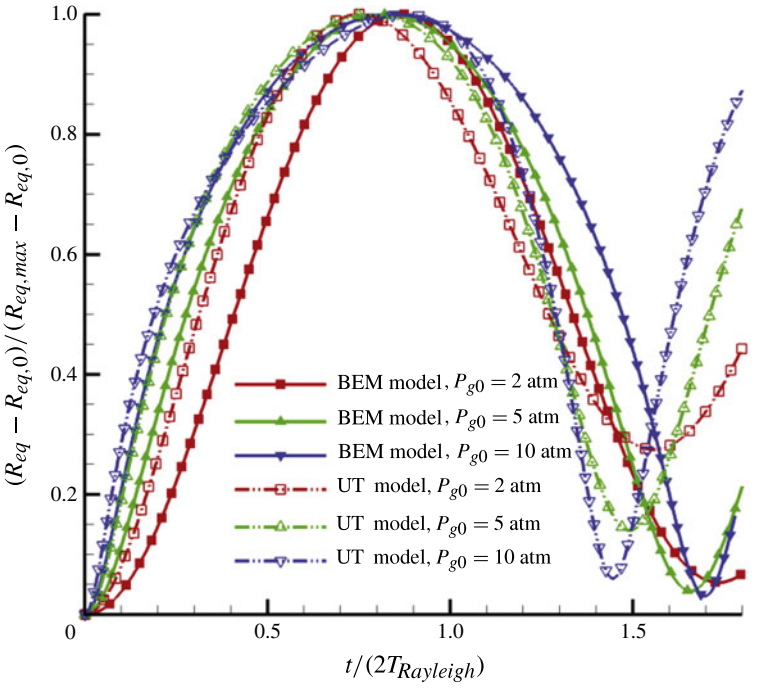


FIGURE 17. (Colour online) Comparison between 3DYNAFS-BEM© and the UT model of the normalized equivalent radius versus time for small bubble oscillations in the case of tandem bubbles subjected to smaller oscillations ($P_{g0} = 2$ atm, 5 atm and 10 atm).

losses due to the compressibility and boundary layer effects that are included in the UT model. However, with tandem bubbles the effects of the neglected compressibility and viscosity appear to have an opposite trend than for single bubbles (figure 6). The percentage deviation between the models for both R_{max} and the period are here reduced as P_{g0} is increased, while for the single-bubble case it was the other way around. Figure 17 shows a normalized plot of bubble equivalent radius versus time for all three cases. Accounting for compressibility and viscosity, as for the single bubble,

https://doi.org/10.1017/jfm.2012.526 Published online by Cambridge University Press

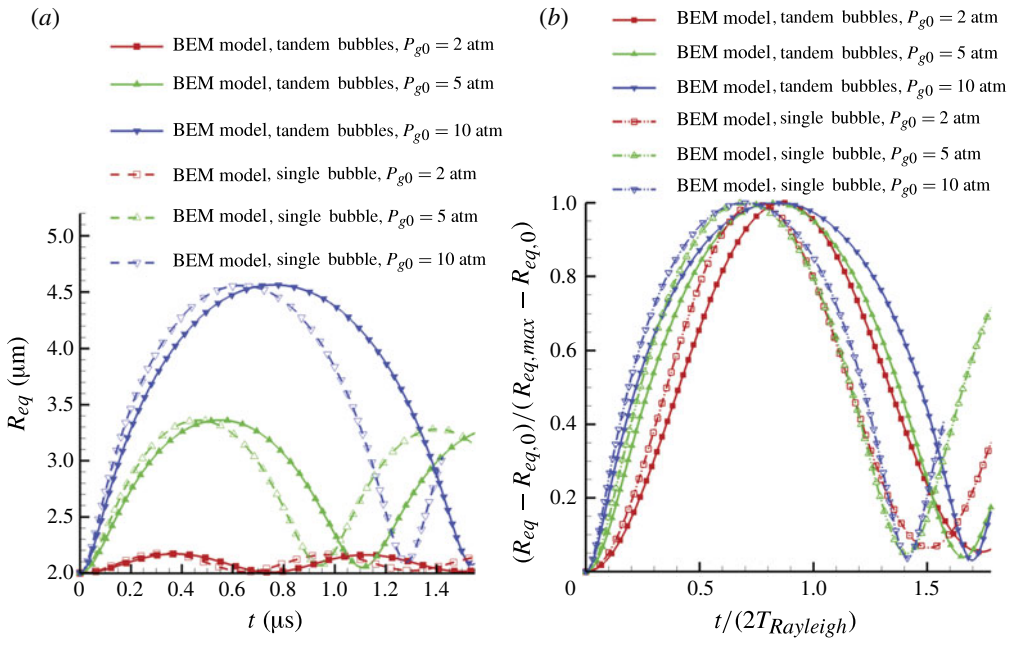


FIGURE 18. (Colour online) Comparison of the dynamics between single bubble and tandem bubbles for small oscillations obtained with 3DYNAFS-BEM© (distance between the bubbles is 40 μm, $H_{gap} = 25$ μm, $R_0 = 2.0$ μm): (*a*) dimensional plots. (*b*) normalized plots.

reduces the maximum radius, reduces the bubble period and increases the minimum bubble radius at the end of the first bubble period, all reflecting loss of energy through radiation and viscosity.

Figure 18(*a*) shows a comparison of the results obtained with 3DYNAFS-BEM© for the equivalent bubble radius versus time between the single-bubble and the tandem-bubble runs. Figure 18(*b*) shows the same results in normalized format. The plots clearly indicate that the presence of the second bubble increases the collapse period of the bubbles, while affecting the maximum bubble radii little, when compressibility and viscous boundary layers are ignored. The normalization shows that the bubble period lengthening increase with P_{g0}, i.e. with the increase of the ratio of R_{max} and the spacing between the bubbles.

4.2.2. *Effect of tandem-bubble interaction on bubble dynamics*

Large-amplitude oscillations of synchronized tandem bubbles, i.e. $R_0 = 2$ μm, $P_{g0} = 886$ atm, were also simulated using BEM model. Figure 19 shows that both bubbles behave identically and form re-entrant jets directed toward each other near the end of collapse. This scenario was not used in the experimental study by Sankin *et al.* (2010) because of its high risk of cell killing.

To illustrate the effect of tandem-bubble interaction on bubble dynamics in the confined domain, R_{max} and bubble period, $T_{collapse}$, obtained from single- and tandem-bubble cases are compared for different driving pressure P_{g0}. It can be seen from figure 20 that the tandem-bubble interaction only has a small effect on the maximum

https://doi.org/10.1017/jfm.2012.526 Published online by Cambridge University Press

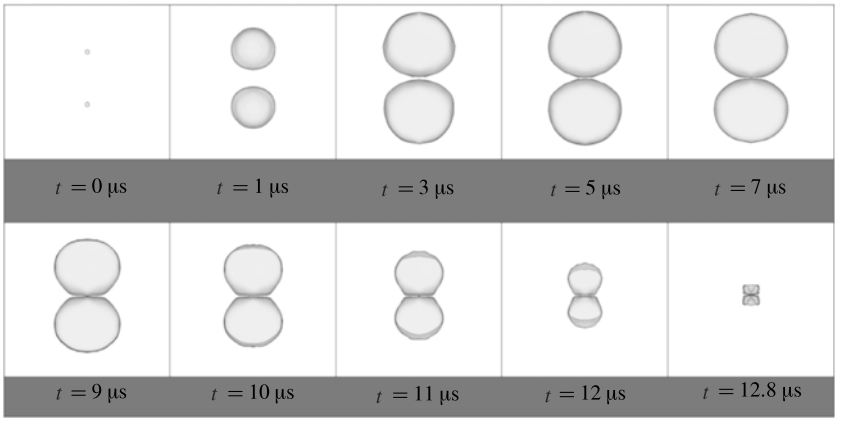


FIGURE 19. Dynamics of synchronized tandem bubbles simulated with 3DYNAFS-BEM©: bubble spacing = 40 μm, $H_{gap} = 25$ μm, $R_0 = 2.0$ μm and $P_{g0} = 835$ atm.

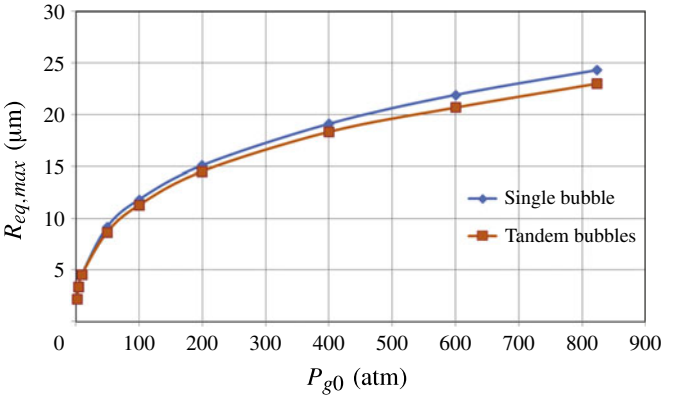


FIGURE 20. (Colour online) Comparison of R_{max} between single- and tandem-bubble cases for different driving pressures, P_{g0} ($H_{gap} = 25.0$ μm, $R_0 = 2$ μm).

bubble size. The difference in R_{max} between single and tandem bubbles is slightly increased from 0.1 % up to 5 % as P_{g0} is increased from 2 to 886 atm.

Figure 21 compares the bubble periods between single and tandem bubbles for different initial internal gas pressures P_{g0}. As P_{g0} increases, the difference in bubble period increases due to stronger bubble–bubble interaction. This is typical for bubble–bubble (or bubble–wall) interaction when the non-dimensional standoff D_{bub}/R_{max} decreases.

4.2.3. *Effect of time delay between two laser-generated bubbles*

Using time-delayed tandem bubbles to enhance bubble pulse has been studied by Chahine (2005). This study showed that the first bubble can be driven to collapse more violently than when isolated by controlling the second bubble delay time. In addition to the bubble pulse, the pressure field generated by the second bubble also significantly alters the local deformation of the first bubble and results in jet formation if the standoff between the two bubbles is small.

https://doi.org/10.1017/jfm.2012.526 Published online by Cambridge University Press

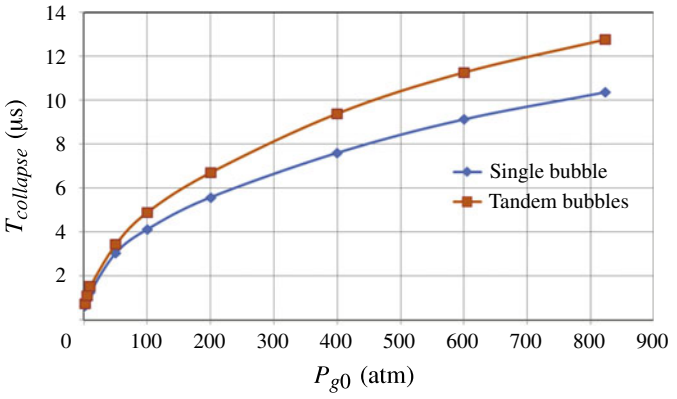


FIGURE 21. (Colour online) Comparison of bubble period between single- and tandem-bubble cases for different initial gas driving pressures, P_{g0} ($H_{gap} = 25.0$ μm, $R_0 = 2$ μm).

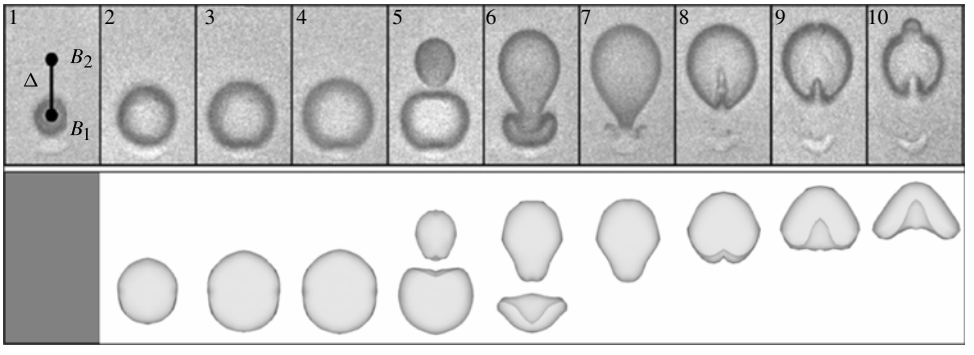


FIGURE 22. Comparison between 3DYNAFS-BEM© and experimental observations of Sankin *et al.* (2010) for the behaviour of tandem bubbles initiated with a delay of 4 μs from 1 μs to 10 μs with a time interval of 1 μs. In simulation bubble spacing = 40 μm; $H_{gap} = 25$ μm; $R_0 = 2.0$ μm and $P_{g0} = 835$ atm.

To highlight the effect of time delay on the jet formation, the dynamics of time-delayed tandem bubbles were obtained by 3DYNAFS-BEM© and compared to experimental observations of Sankin *et al.* (2010). As shown in figure 22, the numerical model clearly demonstrates that the second bubble, generated 4 μs after the first bubble, elongates substantially during its expansion and forces the jet developing in the first bubble to speed up significantly. This resulted in poration of a nearby cell as reported by Sankin *et al.* (2010). Overall 3DYNAFS-BEM© reproduces the observations qualitatively and quantitatively. The calibration of the initial conditions from the single-bubble study appears to enable accurate description of the tandem-bubble cases with delay, as these initial conditions were not tuned at all here.

Figure 23 shows a comparison of the equivalent radii of the two bubbles for the synchronized and time-delayed cases. It is seen that for the case with a delay, before the second bubble is initiated the first bubble behaves simply as an isolated bubble. As a result, this first bubble reaches its maximum size earlier than in the case of the two

https://doi.org/10.1017/jfm.2012.526 Published online by Cambridge University Press

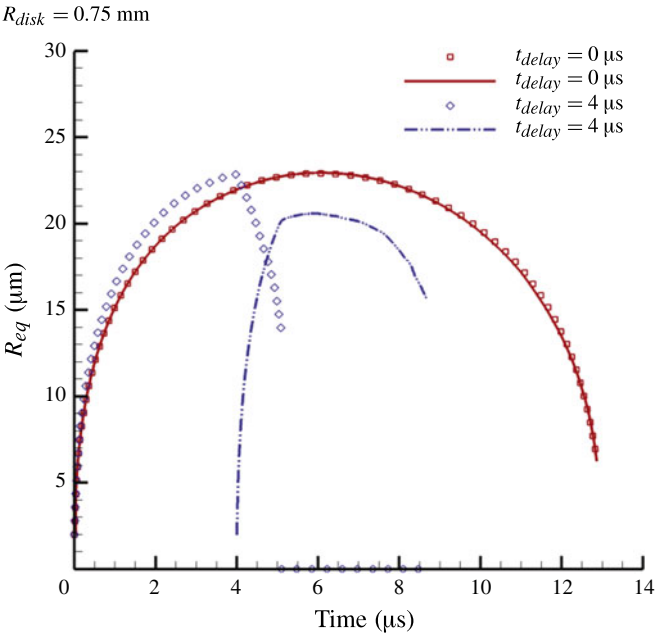


FIGURE 23. (Colour online) Effect of time delay on the equivalent radii of two bubbles generated simultaneously or with a delay of 40 ms: bubble spacing = 40 μm, $H_{gap} = 25$ μm, $R_0 = 2.0$ μm and $P_{g0} = 835$ atm.

synchronized bubbles. However, the growth of the first bubble is interrupted as soon as the second bubble is generated owing to the presence of overpressure imparted by the initial expansion of the second bubble. The interaction of the tandem bubbles not only impedes the first bubble from growing further, but also later the pressure field due to the first bubble collapse prevents the second bubble from reaching its full potential size. Such interactions due to time delay are expected to play a profound role when searching for an optimal condition for jet formation (Yuan, Sankin & Zhong 2011). The present model can be used for such an optimization or for the investigation of other configurations.

4.2.4. *Flow field analysis*

3DYNAFS-BEM© was used to obtain the field pressure contours for the various tandem-bubble cases simulated. Figure 24 shows for synchronized tandem bubbles the time evolution of the pressure field in the centreplane, i.e. at $y = H_{gap}/2$. In all sequences the pressure contours shown use the same colour scales from -2×10^4 to 9×10^4 Pa except at $t = 0.02$, 12.0 and 12.8 μs, where the scale goes from 5×10^5 to 9×10^6 Pa. The higher pressure scale at the beginning and end of the bubble cycle is used to highlight the high pressures in these three sequences. A high pressure field results from initial fast bubble expansion and it decays quickly as the bubble grows. This is followed by a drop of the pressure around the bubble until bubble collapse. During bubble growth the shapes of the two bubbles in the centreplane between the two plates deviate from circular as the inner bubble surfaces approach each other resulting in a higher pressure between the two bubbles. This region disappears as the two bubble surfaces practically touch. During the collapse phase, high-pressure regions form on the outer sides of the two bubbles and help develop the re-entrant jets.

https://doi.org/10.1017/jfm.2012.526 Published online by Cambridge University Press

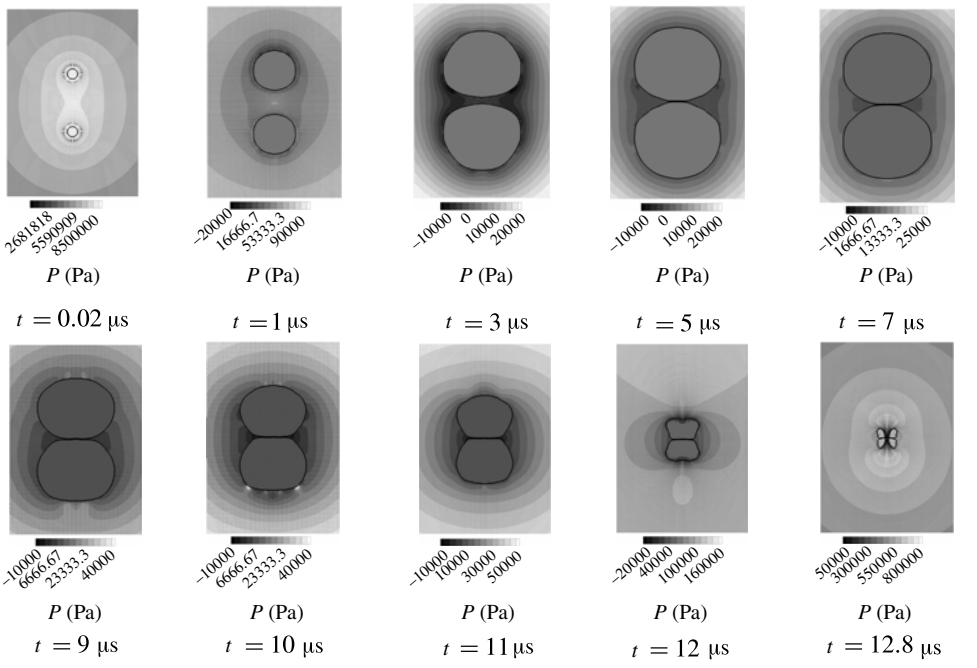


FIGURE 24. Pressure field during the growth and collapse phases of synchronized tandem bubbles as obtained with 3DYNAFS-BEM©: bubble spacing = 40 μm, $D_{gap} = 25$ μm, $R_0 = 2.0$ μm and $P_{g0} = 835$ atm.

Figure 25 shows, for tandem bubbles with a 4 ms delay, sequences of the time evolution of the pressure field in the centreplane between the two plates from 4 to 9 ms. A more detailed time sequence between 4 and 5 ms is shown in figure 26 to illustrate the flow field just after the second bubble is generated. All pressure contours are shown in the same scale from -2×10^4 to 9×10^4 Pa. It is seen that the first bubble, which has grown significantly larger than the second one and is close to its maximum size, acts locally virtually like a free surface. It is pushed in owing to the local high pressure generated by the second explosively growing bubble and its collapse is initiated. This deformation develops into a fast re-entrant jet, which draws in liquid flow behind and elongates the second bubble. The re-entrant jet eventually touches the opposite side of the bubble. The collapse of the second bubble then triggers the formation of a re-entrant jet in the second bubble. Note that in the present computations, the first bubble was deactivated, i.e. its influence was turned off by removing its panel integral contribution to other nodes when the influence coefficients $\bar{A}$ and $\bar{B}$ were computed for (3.8), at the moment when the jet touched the other side of the first bubble. This aspect needs further study and numerical development.

5. Conclusions

We have presented in this communication part of an on-going effort to develop analytical and computational tools to enable the study of the complex interaction between microbubbles and nearby boundaries. We have described the methods used and illustrated this with examples. We have used these examples to discuss some

https://doi.org/10.1017/jfm.2012.526 Published online by Cambridge University Press

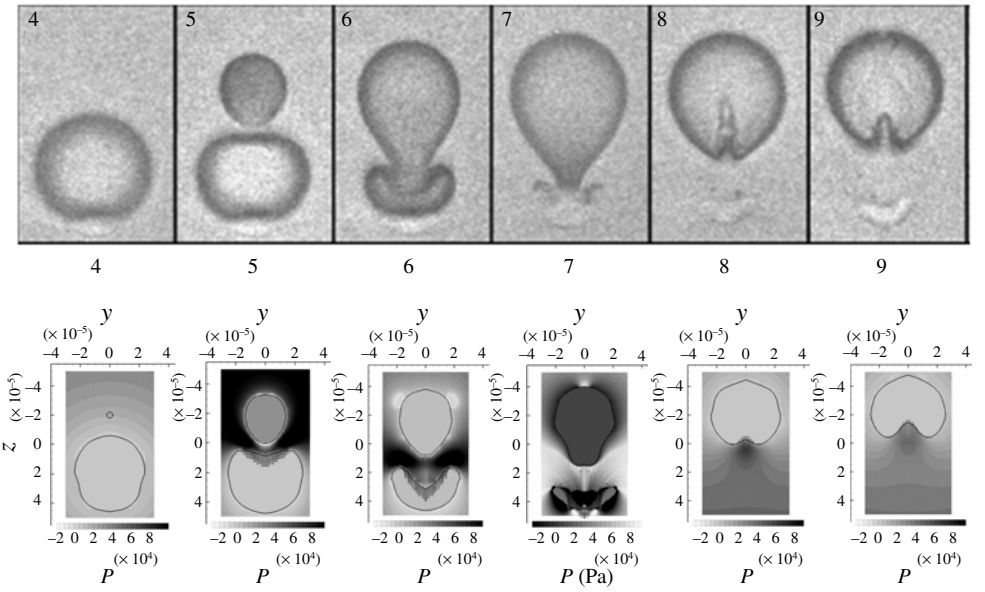


FIGURE 25. Pressure field during various phases of tandem bubbles fired with a 4 μs delay from 4 μs to 9 μs with a time interval of 1 μs corresponding to the experimental observations: bubble spacing = 40 μm, $H_{gap} = 25$ μm, $R_0 = 2.0$ μm and $P_{g0} = 835$ atm.

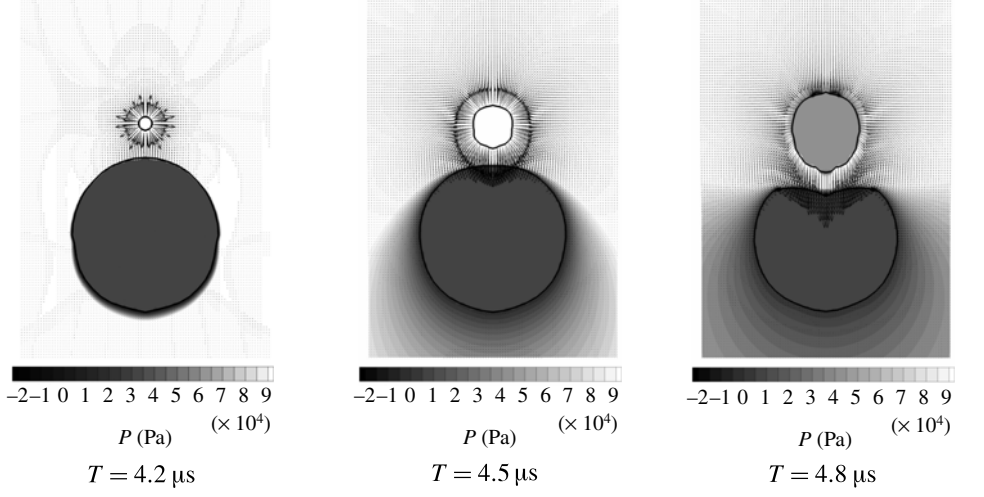


FIGURE 26. Further detail of the pressure field between 4 μs and 5 μs for the same condition as in the previous figure.

physical aspects of the problems studied and compared with existing experimental evidence.

Specific conclusions for the particular study of bubbles between two confining parallel walls are summarized as follows.

(i) For small-amplitude oscillations of a single bubble in an unbounded domain, results from the 3DYNAFS-BEM© and UT model compare quite well both in terms of the maximum bubble radius and bubble period.

https://doi.org/10.1017/jfm.2012.526 Published online by Cambridge University Press

(ii) For small-amplitude oscillations of a single bubble between confined walls, the UT model, which accounts for viscous boundary layers and compressibility of the liquid, predicts a lower maximum equivalent bubble radius, R_{max}, a smaller period for the same initial gas pressure in the bubble, P_{g0}, and a larger minimum bubble radius at the end of the first period. This is attributed to the energy losses enhanced by the presence of the plates and captured in the model accounting for compressibility and viscous boundary layers.

(iii) The differences between the two models can also be attributed to the size of the disk, which is finite in the incompressible model and infinite in the UT model. Computation results and analytical analysis show a noticeable effect of the disk size on the solution.

(iv) Differences between the two models could also be attributed to account for the bubble shape, which for small oscillations corresponding to an initial gas pressure, $P_{g0} = 10$ atm, seem to start playing a role towards the end of the bubble cycle. This effect will increase with an increase in P_{g0}.

(v) For large-amplitude bubble oscillations, the bubble profiles and projected radii predicted by 3DynaFS-Bem© match very well with the corresponding experimental results during all phases of the bubble expansion/collapse, once the bubble maximum radius and the bubble period are matched by varying the disk size, R_{disk}.

(vi) For small-amplitude oscillations of tandem bubbles between plates, the compressible model predicts a lower maximum equivalent bubble radius, R_{max}, a smaller period for the same initial gas pressure in the bubble, P_{g0}, and a larger minimum bubble radius at the end of the first period when compared to 3DynaFS-Bem©. The percentage deviation between the models is reduced as P_{g0} is increased while for the single-bubble case it was the other way around.

(vii) 3DynaFS-Bem© simulations for small-amplitude oscillations of single/tandem bubbles between plates clearly indicate that the presence of the second bubble increases the period of the bubbles, while having little effect on the maximum bubble radii.

(viii) For large-amplitude oscillation of tandem bubbles between plates, 3DynaFS-Bem© reproduces quite well the Duke experimental observations (Sankin *et al.* 2010) qualitatively and quantitatively. 3DynaFS-Bem© also recovers the fact that the second bubble, expanding later after the growth of the first bubble has started to decelerate, causes the jet forming in the first bubble to reach a much larger speed. This effect depends critically on the timing of the second bubble relative to the first and does not exist if the two bubbles are triggered simultaneously.

Overall, we have begun to develop numerical and mathematical models that are aimed at capturing the essential features of single- and tandem-bubble oscillations in a narrow fluid gap confined by two parallel solid boundaries. From a computational point of view, this tandem-bubble interaction in a narrow gap presents a new challenge and also opportunities in modelling the interaction of bubble–bubble boundaries that have not been adequately addressed before. Therefore, complementary approaches that combine numerical and mathematical analysis of the tandem-bubble interaction may provide the most comprehensive and insightful description of the experimental observations. Such an analysis should be valuable in facilitating parametric studies of

https://doi.org/10.1017/jfm.2012.526 Published online by Cambridge University Press

the tandem-bubble interactions involved in single-cell manipulation. It will also help in improving our understanding of the mechanism of cavitation-induced membrane poration, and in optimizing the design of tandem-bubble control for biomedical applications such as in drug delivery and cell therapy.

Acknowledgements

The authors would like to acknowledge support of NIH as well as internal IR and D organizational funds. Work supported by NIH grant nos. 2R44EB005139-02A1 (DFI), DK070618 and EB011603 (UT), DK052985 and RR016802 (Duke).

REFERENCES

ARNDT, R. E. A 1981 Cavitation in fluid machinery and hydraulic structure. *Annu. Rev. Fluid Mech.* **13**, 273–328.

BLAKE, J. R. & GIBSON, D. C. 1987 Cavitation bubbles near boundaries. *Annu. Rev. Fluid Mech.* **19**, 99–123.

BRENNEN, C. E. 1995 *Cavitation and Bubble Dynamics*. Oxford University Press.

CALVISI, M. L., ILORETA, J. I. & SZERI, A. J 2008 Dynamics of bubbles near a rigid surface subjected to a lithotripter shock wave. Part 2. Reflected shock intensifies nonspherical cavitation collapse. *J. Fluid Mech.* **616**, 63–97.

CHAHINE, G. L. 1982 Experimental and asymptotic study of nonspherical bubble collapse. *Appl. Sci. Res.* **38**, 187–197.

CHAHINE, G. L. 1991 Dynamics of the interaction of non-spherical cavities. In *Mathematical Approaches in Hydrodynamics* (ed. T. Miloh). SIAM.

CHAHINE, G. L. 1993 Cavitation dynamics at microscale level. *J. Heart Valve Disease* **3**, 102–116.

CHAHINE, G. L. 1994 Strong interactions bubble/bubble and bubble/flow. In *Bubble Dynamics and Interface Phenomena* (ed. J. R. Blake, J. M. Boulton-Stone & N. H. Thomas). Kluwer.

CHAHINE, G. L. 1995 Bubble interactions with vortices. In *Vortex Flows* (ed. S. Green), chap. 18, Kluwer.

CHAHINE, G. L. 1996 Scaling of mechanical heart valves for cavitation inception observation and acoustic detection. *J. Heart Valve Disease* **5**, 207–215.

CHAHINE, G. L. 2005 Numerical studies of the interaction of multiple explosion bubbles (limited distribution). *Crit. Technol. Shock Vib.* **3** (1), 1–13.

CHAHINE, G. L. & DURAISWAMI, R. 1993 Method for calculating 2-D and 3-D underwater explosion bubble behavior in free water and near structure. *NSWC Dahlgren Div. Rep.* NSWCDD/TR-93/44.

CHAHINE, G. L., DURAISWAMI, R. & KALUMUCK, K. M 1997 Boundary element method for calculating 2-D and 3-D underwater explosion bubble loading on nearby structures including fluid-structure interaction effects. *NSWC Dahlgren Div. Rep.* NSWCDD/TR-93/46.

CHAHINE, G. L., DURAISWAMI, R. & REBUT, M. 1992 Analytical and numerical study of large bubble/bubble and bubble/flow interactions, In *19th ONR Symposium of Naval Hydrodynamics*, Seoul S. Korea, 679–699.

CHAHINE, G. L. & LIU, H. L. 1985 A singular perturbation theory of the growth of a bubble cluster in a superheated liquid. *J. Fluid Mech* **156**, 257–279.

CHAHINE, G. L. & MORINE, A. K. 1980 The influence of polymer additives on the collapse of a bubble between two solid walls. *ASME Cavitation and Polyphase Flow Forum, New Orleans, Louisiana*.

CHAHINE, G. L., PERDUE, T. O. & TUCKER, C. B. 1989 Interaction between underwater explosion bubble and a solid submerged body. *Dynaflow Inc. Tech. Rep.* 89001-1.

CHEN, H., BRAYMAN, A. A., BAILEY, M. R. & MATULA, T. J. 2010 Blood vessel rupture by cavitation. *Urol Res.* **39**, 321–326.

CHEN, H., BRAYMAN, A. A., BAILEY, M. R. & MATULA, T. J. 2011 Observations of translation and jetting of ultrasound-activated microbubbles in mesenteric microvessel. *Ultraso. Med. Biol.* **37**, 2139–2148.

https://doi.org/10.1017/jfm.2012.526 Published online by Cambridge University Press

CUI, J., HAMILTON, M. F., WILSON, P. S. & ZABOLOTSKAYA, E. A. 2006 Bubble pulsations between parallel plates. *J. Acoust. Soc. Am.* **119** (4), 2067–2072.

DARROZES, J. S. & CHAHINE, G. L. 1983 Les Recherches sur le Phenomne de Cavitation Effectues L'Ecole Nationale Suprieure de Techniques Avances. Sciences et Techniques de L'Armement, Memorial de l'Artillerie Francaise, 11–183.

GONZALEZ-AVILA, S. L., KLASEBOER, E., KHOO, B. C. & OHL, C.-D. 2011 Cavitation bubble dynamics in a liquid gap of variable height. *J. Fluid Mech.* **682**, 241–260.

GRACEWSKI, S. M., MIAO, H. & DALECKI, D. 2005 Ultrasonic excitation of a bubble near a rigid or deformable sphere: implications for ultrasonically induced hemolysis. *J. Acoust. Soc. Am.* **117** (3), 1–8.

HAINES, J. R., RIEMER, B. W., FELDE, D. K., HUNN, J. D., PAWEL, S. J. & TSAI, C. C. 2005 Summary of cavitation erosion investigations for the SNS mercury target. *J. Nucl. Mater.* **343** (1–3), 58–69.

HAUBOLD, A. D., ELY, J. L. & CHAHINE, G. L. 1994 Effect of cavitation on pyrolytic carbon in vitro. *J. Heart Valve Dis.* **3**, 318–323.

HAY, T. A., ILINSKII, YU. A., ZABOLOTSKAYA, E. A. & HAMILTON, M. F. 2012 Model for bubble pulsation in liquid between parallel viscoelastic layers. *J. Acoust. Soc. Am.* **132** (1), 124–137.

HSIAO, C.-T. & CHAHINE, G. L. 2010 3DYNAFS© *– A Three-dimensional Free Surface and Bubble Dynamics Code*. Dynaflow, Inc., User Manual 7.085.

HSIAO, C.-T., LU, X. & CHAHINE, G. L. 2010 Three-dimensional modelling of the dynamics of therapeutic ultrasound contrast agent. *Ultraso. Med. Biol.* **36** (12), 2065–2079.

ILINSKII, Y. A., ZABOLOTSKAYA, E. A., HAY, T. A. & HAMILTON, M. F. 2012 Models of cylindrical bubble pulsations. *J. Acoust. Soc. Am.* **133** (3), 1346–1357.

ILORETA, J. I., FUNG, N. & SZERI, A. J 2008 Dynamics of bubbles near a rigid surface subjected to a lithotripter shock wave. Part 1. Consequences of interference between incident and reflected waves. *J. Fluid Mech.* **616**, 43–61.

KNAPP, R. T., DAILY, J. W. & HAMMITT, F. G. 1970 *Cavitation*. McGraw-Hill.

KRIEGER, J. & CHAHINE, G. L. 2005 Acoustic signals of underwater explosions Near surfaces. *J. Acoust. Soc. Am.* **118** (5), 2961–2974.

KRONINGER, D., KOHLER, K., KURZ, T. & LAUTERBORN, W. 2010 Particle tracking velocimetry of the flow field around a collapsing cavitation bubble. *Exp. Fluids* **48** (3), 395–408.

LAUTERBORN, W. & BOLLE, H. 1975 Experimental investigations of cavitation-bubble collapse in the neighbourhood of a solid boundary. *J. Fluid Mech.* **72**, 391–399.

LEIGHTON, T. 2012 The inertial terms in equations of motion for bubbles in tubular vessels or between plates. *J. Acoust. Soc. Am.* **130**, 3333–3338.

LIM, K. Y., QUINTO-SU, P. A., KLASEBOER, E. & KHOO, B. C. 2010 Nonspherical laser-induced cavitation bubbles. *Phys. Rev.* E **81**, 016308.

MIAO, H., GRACEWSKI, S. M. & DALECKI, D. 2008 Ultrasonic excitation of a bubble inside a deformable tube: implications for ultrasonically induced hemorrhage. *J. Acoust. Soc. Am.* **124** (4), 2374–2384.

MILLER, D. L 1987 A review of ultrasonic bioeffects of microsonation, gas-body activation, and related cavitation-like phenomena. *Ultraso. Med. Biol.* **13**, 443–470.

MITRAGOTRI, S. 2005 Innovation healing sound: the use of ultrasound in drug delivery and other therapeutic applications. *Nature Rev. Drug Dis.* **4** (3), 255–260.

OVERVELDE, M., GARBIN, V., DOLLET, B., COJOC, D., FERRARI, E., DE JONG, N., FABRIZIO, E. D., LOHSE, D. & VERSLUIS, M. 2007 3D optical micromanipulation of ultrasound contrast agents: bubble-wall and bubble–bubble interactions. In *Proceedings of the 19th International Congress on Acoustics*, Paper NLA-02-005-IP.

PISHCHALNIKOV, Y. A., SAPOZHNIKOV, O. A., BAILEY, M. R., WILLIAMS, J. C., CLEVELAND, R. O., COLONIUS, T., CRUM, L. A., EVAN, A. P. & MCATEER, J. A. 2003 Cavitation bubble cluster activity in the breakage of kidney stones by lithotripter shockwaves. *J. Endourol.* **17**, 435–446.

PLESSET, M. S. & CHAPMAN, R. B. 1971 Collapse of an initially spherical vapour cavity in the neighbourhood of a solid boundary. *J. Fluid Mech.* **47** (2), 283–290.

https://doi.org/10.1017/jfm.2012.526 Published online by Cambridge University Press

PLESSET, M. S. & PROSPERETTI, A. 1977 Bubble dynamics and cavitation. *Annu. Rev. Fluid Mech.* **9**, 145–185.

SANKIN, G. N., YUAN, F. & ZHONG, P 2010 Pulsating tandem microbubble for localized and directional single cell membrane poration. *Phys. Rev. Lett.* **105** (7), 078101.

SHIMA, A. & SATO, Y 1980 The behaviour of a bubble between narrow parallel plates. *Z. Angew. Math. Phys.* **31**, 691–704.

SHIMA, A & TOMITA, Y 1981 The behavior of a spherical bubble near a solid wall in a compressible liquid. *Ing.-Arch.* **51**, 243–255.

TOMITA, Y., ROBINSON, P. B., TONG, R. P. & BLAKE, J. R. 2002 Growth and collapse of cavitation bubbles near a curved rigid boundary. *J. Fluid Mech.* **466**, 259–283.

TOMITA, Y., SATO, K. & SHIMA, A 1994 Interaction of two laser-produced cavitation bubbles near boundaries. In *Bubble Dynamics and Interface Phenomena* (ed. J. R. Blake, J. M. Boulton-Stone & N. H. Thomas), Kluwer.

WILSON, S. K. 2010 Dynamics of a two-dimensional vapour bubble confined between superheated or subcooled parallel plates. *Phys. Rev.* E **81**, 046314.

YUAN, F., SANKIN, G. N. & ZHONG, P. 2011 Dynamics of tandem bubble interaction in a microfluidic channel. *J. Acoust. Soc. Am.* **130**, 3339.

ZHANG, J., DUNCAN, J. H. & CHAHINE, G. L. 1993 The final stage of the collapse of a cavitation bubble near a rigid wall. *J. Fluid Mech.* **257**, 147–181.

ZHONG, P., COCKS, F. H., CIOANTA, I. & PREMINGER, G. M. 1997 Controlled, forced collapse of cavitation bubbles for improved stone fragmentation during shock wave lithotripsy. *J. Urol.: Invest. Urol.* **158**, 2323–2328.

https://doi.org/10.1017/jfm.2012.526 Published online by Cambridge University Press